Towards heavy metal free quantum dot-based applications

On the photoluminescence line broadening and exciton recombination dynamics of $CuInS_2$ nanocrystals, and the exploration of a synthesis route for InP quantum well nanocrystals

Huygen Job Jöbsis

Supervisors:
P. T. Prins
Dr. C. De Mello Donega

Utrecht University

Condensed Matter and Interfaces
Utrecht University
February 22, 2020

Abstract

For this work we are interested in two heavy-metal free semiconductor nanomaterials that could be incorporated as the fluorophores in luminescent solar concentrators and LEDs; copper indium sulphide ($CuInS_2$) and indium phosphide (InP). For InP NCs we are interested in a relatively new synthesis method of InP quantum well nanocrystals (NCs). For these structures the InP NCs are comprised in the shell, in this way the PL can potentially cover the entire visible spectrum and into the near-infrared (NIR) by controlling the shell thickness. The synthesis method proved to be very complicated and no proof of a successful synthesis was obtained. Characteristic for CIS NCs is a broad photoluminescence (PL) bandwidth, this is disadvantageous for its potential application in LSCs. A thorough understanding of the nature of this broad band could provide insights on ways to narrow the PL band. Different line broadening effects are studied using various ensemble techniques and single particle spectroscopy. The results of these experiments indicate that the broad PL bandwidth observed for CIS NCs partly arises due to inhomogeneities in the sample. Single particle spectroscopy substantiates this claim, by showing strongly decreased PL bandwidths at the single particle level. Nevertheless, this reduced bandwidth is still considerably broader than observed for their cadmium-containing analogues. As such part of the broad PL band is intrinsic to the material as well. To study the fundamental principles behind this broad intrinsic PL bandwidth, the exciton recombination pathways in CIS NCs is studied using power dependent transient absorption spectroscopy. With the results of these experiments we reproduce the experimental proof for the two-fold degeneracy of the quantized electron in the CB, identifying the hole as the localized carrier in the exciton recombination process. In addition, the TA data shows a blueshift of the bleach signal upon increasing the pump power. We attribute this shift to fast non-radiative Auger recombination of e-h pairs with a good wavefunction overlap in the multi-exciton regime, leaving the energetically higher excitons thus shifting the bleach signal to the blue. To validate this idea the experiment described in this work have to be repeated using different CIS NCs samples in order to exclude the contribution of the large size distribution to the observed blueshift.

Contents

1. Introduction

Quantum dots (QDs) are nanometre sized crystalline semiconductors ranging from a few hundred to a few thousand atoms each[1]. Due to their tiny dimensions they possess unique characteristics arising from both the atomic and macroscopic world. Where in the bulk regime the optical and electronic properties of a material only depend on its composition, in the nano-regime the size and shape influence the optoelectronic properties as well. These additional degrees of freedom give rise to unique properties like size-dependent light absorption and emission, making this class of materials interesting for a vast range of applications. For this thesis we are interested in two types of applications: luminescent solar concentrators (LSCs) and light-emitting diode (LEDs). LSCs are transparent devices that absorb parts of the solar spectrum and re-emit the energy as red-shifted photons that are guided by total internal reflection towards photovoltaic (PV) cells at the edges of the device. Being transparent this technology can be used energy harvesting windows. LSCs harvest and concentrate solar energy and convert it in an electrical current, while maintaining the original function of letting visible light through and isolation. The second application of interest, LEDs, produce artificial light through an electroluminescent material that converts electricity to light. Additional phosphors can be used to tune the emission wavelength, making LEDs suitable for displays as well.

Figure 1 shows a simple schematic of both applications. In LSCs, QDs could function as the fluorophores (A) that absorb parts of the solar spectrum and re-emit red-shifted photons towards the PV cells. Different QDs can in turn be used as the photosensitive material (B) that converts light to an electric current in PV cells (Fig. 1A). QDs can also be used as the electroluminescent material (C) and phosphors (B) that convert an electrical current into light of a distinct wavelength in LEDs (Fig. 1B). The wide applicability of these nanocrystals (NCs) demonstrates the potential and relevance of QD research[2]. Despite numerous practical device demonstrations, a number of challenges have to be addressed before the full potential of QDs can be unleashed for everyday applications like windows and computer screens. First of all, environmental and health issues have to be considered. Many applications have already been realized using NCs containing heavy metals like cadmium and lead[3–5]. This has motivated a worldwide research effort to heavy metal free alternatives.

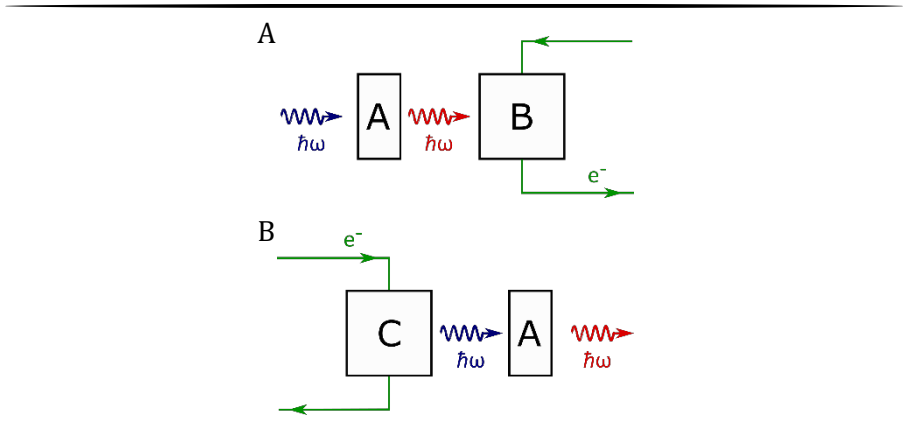

Figure 1 · Schematic representation of energy conversion in LSCs and LEDs. **A.** LSCs generate electricity from light using a fluorophore (B) that absorbs part of the sunlight and re-emits it at another wavelength towards a PV material (A). The PV material which converts it into an electrical current. **B.** In LEDs an electroluminescent material (C) converts electricity into light. An additional fluorophore (B) can be introduced to tune the emitted light to a desired colour. The figure was reproduced from ref [2].

For this thesis we are interested in two materials that show the most promising results as potential substitutes for the fluorophores described in part A of figure 1; copper indium sulphide ($CuInS_2$) and InP NCs[6]. Despite the great potential, a lack of understanding of the photophysics and synthesis methods put the application of these materials still years ahead.

What InP NCs concerned we are interested in a relatively new synthesis method of InP quantum well NCs (chapter 3). For these structures the InP NCs are comprised in the shell, in this way the PL can potentially cover the entire visible spectrum and into the near-infrared (NIR) by controlling the shell thickness.

Chapter 4 provides a thorough analysis of the heating up synthesis of CIS NCs and its scalability. The synthesized CIS NCs are characterised using electron microscopy, small- and wide-angle x-ray scattering. To enhance the optoelectronic properties of CIS NCs we assess the influence of thick CdS shell growth around the CIS core NCs.

Characteristic for CIS NCs is a broad photoluminescence (PL) bandwidth, this is disadvantageous for its potential application in LSCs. A thorough understanding of the nature of this broad band could provide insights on ways to narrow the PL band. Different line broadening effects are studied using various ensemble techniques and single particle spectroscopy (chapter 5).

The broad PL bandwidth appears to arise partly from inhomogeneities in the sample and is partly intrinsic to the material. To understand the fundamental principles behind this intrinsically broad PL band the excited state dynamics of CIS NCs are studied using power dependent transient absorption spectroscopy (chapter 6).

In chapter 7 all our findings are summarized and an outlook for further research is provided.

2. Theoretical background

In this chapter the theoretical background necessary to understand this thesis is provided. In the first section (2.1.) the reader is introduced to the underlying chemistry and physics that give rise to the unique optoelectronic properties of QDs. The unique properties of CIS and InP that differentiate them from other QDs are discussed in section 2.2.. Finally, we provide a brief introduction (2.3.) to two applications that are potentially interesting for CIS and InP QDs; luminescent solar concentrators and light emitting diodes.

2.1. Chemistry and physics of semiconductor nanocrystals

In this section the relevant chemistry and physics necessary to understand the work presented in this thesis is discussed. First the phenomena that give rise to the unique optoelectronic properties of QDs are explained, followed by an introduction to the exciton dynamics in QDs and how they can be influenced by creating heteronanocrystal structures.

2.1.1. Semiconductor nanocrystals

Over the past decades, the interest in the synthesis and characterisation of colloidal semiconducting nanocrystals, also known as quantum dots, has grown immensely. Different to the macroscopic world, when scaling down to the nano-regime some intrinsic properties of such nanoparticles become dependent on their size, shape and composition[1,7–9]. Over the years great control was gained over the synthesis of quantum dots and thus over their properties, making this class of tuneable materials interesting for a wide range of applications and technologies[10–14]. Two phenomena lay the fundaments of this size-dependent behaviour: (1) the large surface to volume ratio and (2) the spatial confinement of charge carriers due to the small dimensions of the particles[1].

When decreasing the size of an object the surface area increases relative to its volume. So, surface atoms play an increasingly more important role in determining the properties of a material when scaling down to the nanoscale. Surface atoms have fewer neighbours limiting the possibility to completely fill its bonding orbitals. Due to these unsatisfied orbitals, also known as dangling bonds, the atoms free energy, reactivity and mobility is increased. The contribution of the surface

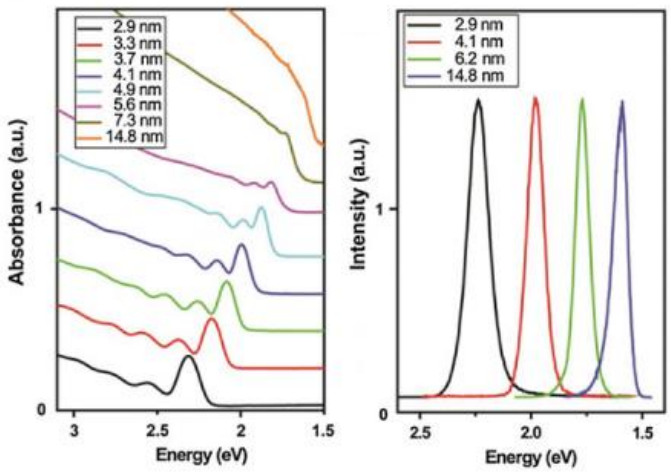

Figure 2 · The absorption and emission spectra for different sizes of CdTe QDs. Increasing the QD size redshifts the absorption and emission spectra due to the decreasing bandgap. The figure was reproduced from ref[1].

atoms to the particles total free energy becomes increasingly more important when decreasing its size, causing some of its properties to change[1,8,9].

The second phenomenon can be understood by considering the electronic band structure of quantum dots. For bulk semiconductors the electronic band structure comprises two bands of energy states. The lower band lies below the Fermi level, i.e. all energy states are occupied by electrons, and is known as the valence band (VB). The second band, the conduction band (CB), lies above the fermi level and is completely empty. The energy gap separating the two bands is referred to as the bandgap (E_g). When irradiated with light of equal or larger energy than the bandgap energy a QD can absorb a photon. The photon excites an electron from the VB to the CB, leaving a positively charged hole in the VB. Due to their opposite charges the electron and hole bind through a Coulomb potential forming a quasi-particle that is usually referred to as an exciton. The wavefunction describing the exciton has a certain spatial extension, called the exciton Bohr radius (a_0), and is characteristic for the material. When the size of a QD is reduced to dimension similar to or smaller than a_0, the exciton is confined in the NC. The effect of confinement becomes immediately clear when looking at the Brus formula[15]. This formula is an approximate solution of the Schrödinger equation considering a spherical semiconductor nanocrystal of radius r. Assuming infinite potential well boundary conditions, the solution becomes:

$$E_g = E_{g,bulk} + \frac{\hbar^2 \pi^2}{8 m_r r^2} - \frac{1.786 e^2}{\epsilon r} \qquad (1)$$

with m_r the reduced exciton mass and ϵ the dielectric constant of the semiconductor. From this equation it is easily derived that reducing the NC size causes an increase in energy of the material bandgap. As a result, by controlling the size one can tune at what wavelengths the NC absorb and emit light. Figure 2 shows the tunability of the absorption and emission wavelengths of CdTe nanocrystals. The emission and absorption spectra are redshifted upon increasing the particle size as the bandgap decreases. Furthermore, distinct peaks in the absorption spectrum are observed for small NCs. These peaks gradually disappear when increasing the QD size. The nature of these distinct peaks can be explained using linear combination of atomic orbitals (LCAO)

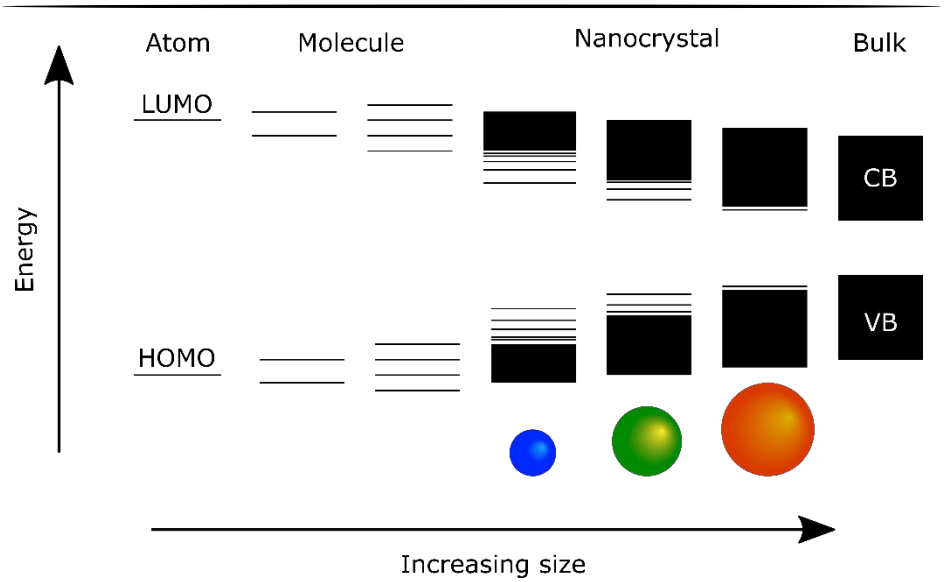

Figure 3 · Schematic representation of the changing electronic structure upon increasing a particle's size starting at the atomic level and ending in the bulk regime. Increasing the NC size decreases the bandgap, thus altering the optical properties. Less discrete energy levels appear at the band edges upon increasing the particle size. The figure was reproduced from ref. [1].

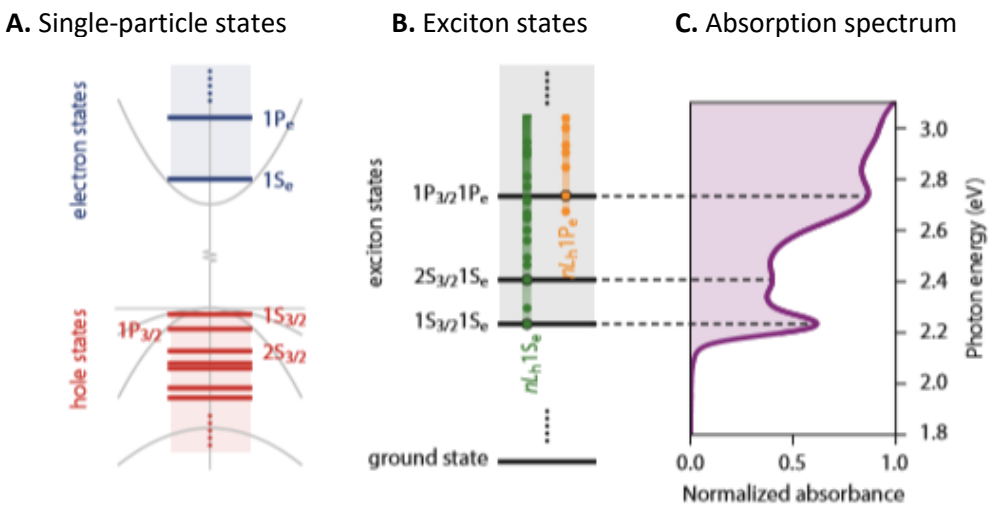

Figure 4 · A. Electron and hole states in a single spherical CdSe QD with their corresponding labels. **B.** Exciton states described as combinations of electron and hole states. **C.** The linear absorption spectrum of a CdSe QD relating distinct energy peaks to transitions between the ground state and different exciton states. The figure was reproduced from ref. [2].

theory. According to LCAO theory two atomic orbitals (AO) combine to form an energetically lower bonding molecular orbital (MO) and an energetically higher anti-bonding MO. For molecules the highest occupied orbital is called the HOMO and the lowest unoccupied orbital the LUMO. Increasing the number of atoms leads to an increase in the number of bonding and anti-bonding MOs, narrowing the energy gap between these states. In the bulk regime the number of MOs is so high that the energy levels can no longer be distinguished, forming a continuum of energy states (Fig. 3). Considering QDs consist of a few hundred to a couple thousand atoms the electronic structure lies in between the bulk and molecular limit[1]. For a QD, the density of MOs is highest in the middle of each band. Moving away from the middle of the bands the density of MOs decreases resulting in discrete energy levels at the band edges[1,9]. The energies corresponding between specific electron and hole states were related to the distinct peaks in the absorption spectrum. The peaks correspond to the transition from a discrete hole state to a specific electron state. In the strong confinement regime, such transitions are described by exciton states. Each exciton state is labelled by combining the label of the specific hole and electron state it arises from. Figure 4 shows how, for CdSe QDs, the exciton states correspond to distinct peaks in the absorption spectrum and from which discrete electron and hole states they arise from. The electron and hole states are labelled using a capital letter which is preceded by a numerical index. The letter represents the angular momentum of the envelop wavefunction (S for l=0, P for l=1, D for l=2, etc.) and the index accompanying the letter denotes the number of the state of a given symmetry. The subscript represents the orientation of the electron spins.

2.1.2. Exciton recombination and lifetime

When photons of a higher energy than the bandgap are absorbed so called hot carriers are formed. The electron and hole occupy excited states above the 1S level (first exciton state). Usually, the excess kinetic energy is quickly dissipated through phonon collisions or non-radiative decay, and the hot exciton relaxes, or cools, to the band edges[16–19]. Such intraband relaxation events are not constrained by the optical selection rules, which is why they proceed on very fast timescales (< 1ps). Once in the 1S state the exciton can only further relax by recombination of the electron and hole. This exciton recombination can either be radiative or non-radiative.

For radiative recombination the exciton energy is emitted as a photon. In most cases the energy of the emitted photon corresponds to the bandgap and is observed as a well-defined peak in the emission spectrum. However, defect states present in the bandgap can trap the charge carriers. These trap states arise either at the surface, e.g. through dangling bonds, or inside the QD through lattice defects[1]. The localization of the carriers in such trap states decreases the overlap of their wavefunctions making radiative recombination less likely. The trapped exciton is now prone to coupling to local vibrations or energy transfer and recombines non-radiatively, i.e. the exciton energy is released as phonons or lattice vibrations[16,17].

The rate at which the competing radiative and non-radiative events proceed can be studied by considering the population change of the excited state over time. In the simplest case where there is no non-radiative decay, i.e. for every photon absorbed a photon is emitted, the population decay follows a single exponential trend:

$$N(t) = N_0 e^{t/\tau} \tag{2}$$

where t is the elapsed time after excitation, τ the exciton radiative lifetime and N_0 the population of the emitting state at t=0. When non-radiative recombination does contribute to the exciton relaxation, the total decay rate will have multiple terms and thus show multi-exponential decay:

$$\tau = \frac{1}{k_{rad}} + \frac{1}{k_{nonrad}} \tag{3}$$

where k_{rad} is the radiative decay rate and k_{nonrad} the non-radiative decay rate. For biexponential decay the data can be fitted using a biexponential fit containing a radiative and non-radiative lifetime. Multiexponential decay requires more complex models to resolve the radiative and non-radiative lifetimes. An estimate of the radiative lifetime in semiconductor NC can be obtained using the following formula[20,21]:

$$k_{rad} = C\lambda^{-1}\rho K \tag{4}$$

where C is a material specific pre-factor, λ the emission wavelength, ρ the density of optical states experienced by the exciton and K the electron-hole overlap integral squared[22]. As C, ρ and K depend on various factors, e.g. the exciton fine structure[20], the refractive index of the medium, the NC shape, the energy band alignment[22], often a simpler approximation is used to get an idea of the radiative decay rate. A rough estimate of the lifetime can be made by determining when the excited population has decayed to 1/e. This approximation gives a quantitative idea of the radiative lifetime of the sample and is used in this thesis.

The ratio between the radiative and non-radiative decay events, i.e. the ratio between the number of emitted and absorbed photons, is reflected in the photoluminescence quantum yield (PLQY), η:

$$\eta = \frac{k_{rad}}{k_{rad}+k_{nonrad}} \tag{5}$$

This measure is relevant to assess the applicability of the material for applications like LSCs and LEDs, as the efficiency of the devices partly rely on the amount of light produced.

2.1.3 The Auger effect

For charged NCs and/or in the multi-exciton regime Auger decay is an important non-radiative recombination process[22]. In this process an exciton collides with a free carrier or a second exciton and transfers its energy thus promoting it to a higher energy state. The promoted carrier usually relaxes back to the band edge resulting in energy loss as heat (hence a non-radiative process).

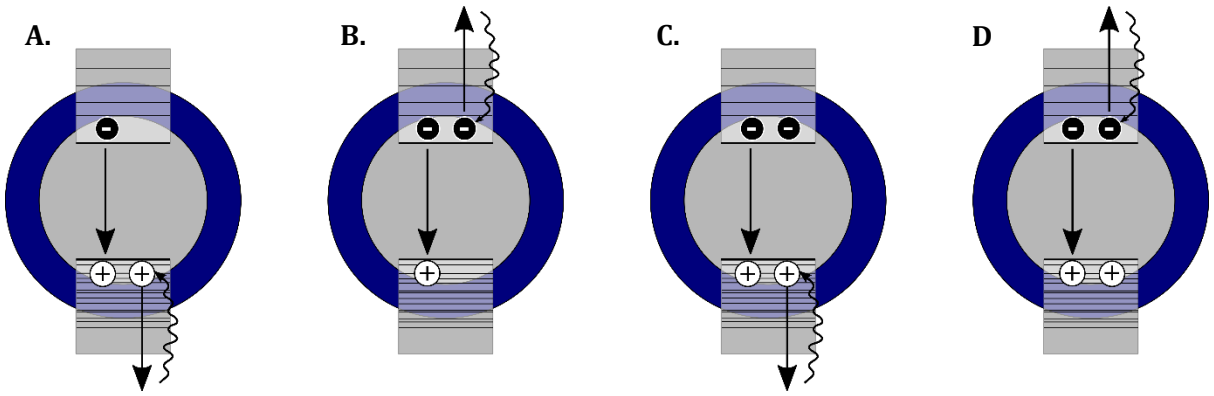

Figure 6 · A. Schematic representation of a positive trion state, where the exciton energy is transferred to the hole. **B.** Schematic representation of a negative trion state, where the exciton energy is transferred to the electron. The schematic representations of the biexciton states which are likely to undergo Auger decay. For **C.** the exciton energy excites the electron into the VB and for **D.** the electron of the second exciton is excited into the CB. The figure is reproduced from ref [2].

Figure 5 shows a schematic representation of the two NC states likely to undergo Auger decay: the trion and the biexciton state. In a charged NCs the trion state can be positive or negative depending if the exciton collides with a positively charged hole or negatively charged electron (figure 5AB). In the biexciton state the recombination energy of the first exciton is transferred to either the hole or to the electron of the second exciton (figure 5CD). Due to quantum confinement carrier wavefunction contain many spatial frequency components. As such the momentum selection rule is relieved for a NC compared to the bulk regime[22]. As a consequence, the Auger decay rate is strongly dependent on the overlap of the electron and hole wavefunctions[18,23,24].

2.1.4. Heteronanocrystals

The optoelectronic properties of QDs can be further tuned by creating heteronanocrystal structures instead of single composition particles[1]. In heteronanocrystals two or more materials are joined in one nanoparticle separated by different heterointerfaces. The energy level alignments of the semiconductor materials at this heterointerface influences the spatial extension of the charge carriers in the NC after photoexcitation. In other words, the energy offset

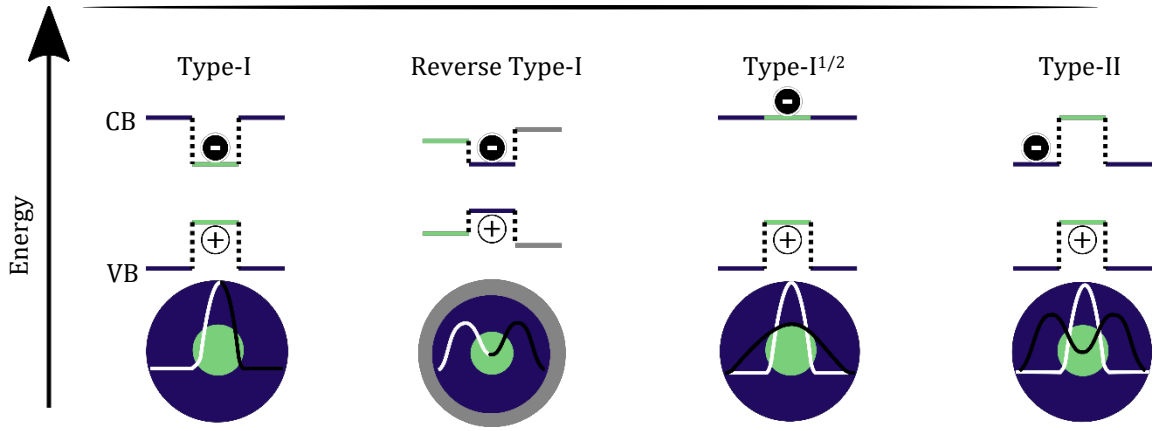

Figure 6 · Schematic representation of the limiting cases in energy level alignments in core/shell heterostructures. For type-I bother carriers are localized in the core, while both carriers are localized in the shell for reverse type-I. In the type-I$^{1/2}$ regime one carrier is localized while the other is delocalized over the entire heteronanocrystal. For the type-II regime the carriers are spatially separated, i.e. one resides in the core while the other is localized in the shell. The figure was reproduced from ref. [1].

determines the localization of the charge carriers in the excited state. Three types of energy level alignments can be identified: type-I, type-I$^{1/2}$ and type-II[25–27]. In the case of type-I energy level alignment, a shell of a wider bandgap material encapsulates the core. In this way, upon photoexcitation the electron and hole are both localized in the core as this is the lowest energy configuration. A special case in the type-I regime is the spherical quantum well. This system comprises a core of a wide bandgap material encapsulated by a smaller bandgap material, which in turn is overcoated by another even wider bandgap material to passivate the surface. As such, both charge carriers are localized in the shell instead of the core. Which is why spherical quantum well systems are also referred to as reverse type-I band alignments. For the Type-II regime the carriers are spatially separated. The energy level alignment localizes the electron in the shell while the hole is localized in the core or vice versa. For the Type-I$^{1/2}$ regime, one of the carriers is localized while the other is delocalized over the entire heteronanocrystal. Figure 6 schematically represents the consequences of the different regimes found in QDs.

2.2. CIS and InP NCs put into perspective

Years of QD research has led to great control over Cd- and Pb-chalcogenide based NCs. Due to the inherent toxicity of these materials their large-scale application is severely hindered. As a result, there is a growing request for heavy-metal free alternatives. CIS and InP QDs show promising PL properties that potentially allow them to substitute their Cd- and Pb-chalcogenide analogues. In this section the state of the art of both CIS and InP QDs is outlined to demonstrate their potential and identify challenges that have to be overcome.

2.2.1. Synthesis of CIS NCs

The CIS NCs, studied in this thesis, are synthesized using the heating up method[28]. Following this method the cation and anion precursors are mixed in a reaction flask and quickly heated up to achieve a supersaturation necessary for NC nucleation[1]. An advantage of this method over more conventional methods like the hot injection method, is that it does not require precursor injection. Interesting for the scalability of this synthesis is the multifunctional use of the precursors. The method described in ref [29] uses an anion precursor that can simultaneously act as ligand and solvent. In this way the more expensive cation precursors react almost completely, and minimal solvent waste is produced[29]. To improve the PLQY CdS or ZnS shells are grown via slow precursor injection. In literature PLQYs over 80% are reported for these core/shell systems[30]. The single step core NC synthesis, high yield, minimal solvent waste, and simple shell overgrowth make this method very scalable and thus a feasible option for large-scale production of CIS QDs needed for applications.

2.2.2. Optical properties of CIS NCs

The PL of CIS NCs can be tuned over the entire visible spectrum into the near-infrared (NIR). The QDs are characterised by a broad PL band, large “global” Stokes shift, featureless absorption spectra and slow multiexponential decay rates. The term global Stokes shift is introduced as the conventional Stokes shift refers to the energy difference between the absorption and emission maxima of the same electronic transition[6]. For CIS NCs the absorption and emission spectra do not originate from the same energy states, so speaking of a Stokes shift would be incorrect. The PL over a wide spectral range in combination with the large global Stokes shift make CIS NCs interesting alternatives for the established class of II-VI and IV-VI compounds.

Different to the binary II-VI and IV-VI compounds the optoelectronic tunability of CIS does not only arise from quantum confinement. The composition of Cu-III-VI_2 materials is much more flexible. Where II-VI and IV-VI compounds do not tolerate large deviations from the ideal

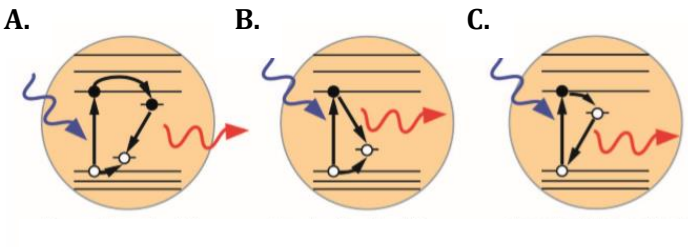

Figure 7 · Schematic representation of the different recombination pathways in $CuInS_2$. **A.** The exciton recombines following the same pathway as in bulk, involving native point defects. **B.** The recombination of a quantized CB electron with a localized hole. The hole is either localized at a lattice defect site or a Cu atom. **C.** The recombination of a localized electron with a hole in a quantized state in the VB. The figure was reproduced from ref. [6][6].

stoichiometry, CIS accommodates a relatively large off-stoichiometry[31,32]. This directly influences the electronic band structure of CIS, as the upper VB arises primarily from Cu 3d orbitals and the CB is constructed from the Cu 4s orbitals mixed with the p orbitals of the chalcogens[33]. As such, large deviations from the ideal $CuXA_2$ formula will significantly influence the bandgap and thus the optoelectronic properties.

Despite extensive research efforts the nature of broad PL band and the featureless absorption spectrum are still poorly understood. One could explain these characteristics due to the poor quality of the synthesis methods resulting in polydisperse products[6]. However, years of research have resulted in a significant improvement of the preparations of these QDs, narrowing the size and shape dispersion to a typical value of 10%[29,34]. Despite these small size and shape dispersion values no clear features in the absorption or narrow emission peaks have been observed, which could mean that these characteristics are intrinsic properties of the material. The exciton recombination pathway that gives rise to these unique optical properties is not (yet) fully understood, in fact there is still a strong division in the scientific community regarding the right model describing exciton recombination[6]. Figure 6 shows the different models designed to describe the exciton recombination in CIS NCs. The simplest model is that the follows the same recombination pathway for CIS NCs is the same as in the bulk regime[35]. In the bulk both charge carriers localize at native point defects, explaining the large stoke shift and broad emission. This model, however, does not explain the size dependence of the emission and absorption. In order to account for the size dependency, one of the charge carriers has to be localized while the other extends through the whole nanoparticle. Some studies argue that the electron localizes at native point defects and radiatively recombines with quantized hole states[36,37], while others propose that the recombination pathway follows a quantized electron in the CB to a localized hole[29,38]. Presently, there is a growing consensus that the latter model describes the exciton recombination in CIS the most accurate. Details of the mechanism are, however, still the cause of strong debates.

Two research groups conducted magnetic circular dichroism measurements on CIS. Their results support the localized hole model, however, their interpretation of the nature of the hole localization differs. Klimov *et al.* argues that the hole localizes at native core defects[29]. While the Gamelin group claims that the hole localizes at a regular Cu^+ ion due to strong hole-phonon coupling and large nuclear reorganization energies upon localization[38]. More recent work by Berends *et al.* reports new findings strongly supporting the latter model[30]. In chapter 6 we will go into more detail of their work and introduce new arguments suggesting the presence of preferential localization sites. Understanding the exciton recombination for CIS QDs also provides insight into the optoelectronic properties of other QDs, as strong similarities between the PL properties of CIS NCs and other Cu-doped nanomaterials are reported in literature[38–40]. Besides

being important from a fundamental viewpoint, fully understanding the recombination pathway is important for its potential incorporation in applications.

2.3.2. InP core/shell NCs

Due to the advances of QD-based applications in the display and lighting industry the demand for a less toxic material to substitute CdSe is high. The most promising alternatives for these applications are the III-V compounds with indium phosphide (InP) having the most potential. InP is a luminescent material with a high PL QY and a good photostability[41]. The synthesis poses a problem though. The current synthesis route relies on the hot-injection method, however, it proves to be difficult to separate the nucleation and growth stage, i.e. growth of InP NCs is accompanied by the nucleation of new particles[42–44]. As a result, a large size distribution is encountered when using this method. From the Brus formula (eq. 1) it follows that the optical bandgap is very sensitive to the QD size. Small variations in size give rise to significant variation in the bandgap and thus in the absorption and emission energy. So, in a polydisperse sample the emission feature is smeared out. This example of inhomogeneous line broadening is detrimental for application in high quality lighting. In the lighting industry, narrow emission peaks are desired in order to attain a high colour purity. It is therefore crucial to obtain as much control as possible over the NC synthesis to limit the size dispersion leading to inhomogeneous broadening. Another problem that limits the InP application for LEDs is associated with its synthesis as well. As already said above, using the current synthesis method, growth of existing InP particles goes hand in hand with the nucleation of new particles. This introduces a certain upper size limit, making it impossible to grow big InP particles[43]. Due to this bottleneck different materials emitting in the red are required as the InP PL does not cover this part of the spectral range. There is therefore a need for an improved or new synthesis method facilitating the production of a more monodisperse InP sample covering the entire visible spectrum.

2.3. Quantum dot based LSCs and LEDs

In this section we discuss two potential applications in which the two materials of interest can be incorporated. First, we will give a brief introduction to luminescent solar concentrators and motivate why CIS NCs are so interesting for this particular application. Followed by a brief introduction to QD-based LEDs.

2.3.1. Luminescent solar concentrators

The conversion of sunlight to an electrical current plays a key role in the public desire for a green and sustainable energy supply in the near future. As a result of decades of research, solar cell efficiencies are high and the manufacturing costs have dropped significantly, enabling the construction of energetically self-sufficient (small) buildings[45]. However, in densely populated areas the rooftop surfaces, where the solar cells are usually installed, become increasingly insufficient to meet the energy demand of an entire skyscraper. This makes it difficult to meet the 'nearly zero energy building' agreement issued by the EU, which requires all public and private buildings to be energy neutral by December 2050[46]. An application that could aid in realizing these ambitious objectives are luminescent solar concentrators (LSCs)[47–50]. An LSC is a transparent material that absorbs parts of the solar spectrum and converts it in an electrical current. A waveguide embedded with highly emissive fluorophores absorbs the solar photons which are re-emitted towards photovoltaic cells (PVs) mounted at edges of the device. As the surface area exposed to the sunlight is much larger than the device edges, an LSC concentrates the photon flux incident on the PVs which increases the external quantum efficiency (EQE). As these devices are semi-transparent, they could redefine the function of a window. Where a conventional window is used as a medium to let visible light in an LSC concentrates parts of the solar spectrum and converts it in an electrical current while maintaining its original function. As such the sides of buildings are transformed in energy harvesting cells. Figure 8 shows a schematic representation of an LSC.

When, in 1976, the concept of an LSC was first introduced QDs were still to be discovered[47]. So, for a long period of time different kinds of fluorophores were explored like organic dyes. These dyes, however, were shown to be far from ideal, due to their small Stokes shift and limited coverage of the solar spectrum[48]. On top of that, the PL of such dyes is low at the near-infrared (NIR) wavelengths, which is where the EQE of Si PVs is the highest. The tuneability of the

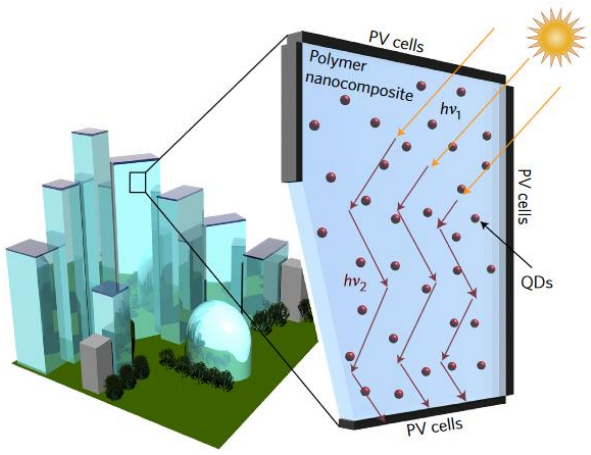

Figure 8 · Schematic representation of an LSC window with QDs as fluorophores. The figure was reproduced from ref. [52][51].

absorption and emission over a wide spectral range, a good photostability and solution-based synthesis, make QDs a very suitable alternative for organic dyes[10,51–53].

One of the major loss mechanisms in LSCs is reabsorption, where a re-emitted photon is absorbed by a second fluorophore[48,53,54]. This second absorption event increases the probability of non-radiative recombination, thus lowering the devices EQE. A large Stokes shift, i.e. a small overlap of the absorption and emission spectra, is desired in order to minimize efficiency loss through reabsorption. Standard core only CdSe and PbS NCs have, like organic dyes, a small Stokes shift. LSCs based on such QDs were shown to have similar or even worse optical losses to reabsorption as some dyes[48,55,56]. Specially engineered heterostructures have shown to tackle these reabsorption losses[56] by, e.g. growing a very thick CdS shell around conventional CdSe cores a quasi-type-II system is formed[57–59]. The CBs of CdSe and CdS align rather well allowing the electron to be localized over the entire particle. However, the offset between the VBs is large, localizing the hole in the CdSe core. Due to the very thick shell, the absorption is dominated by CdS. The rapid localization of the holes to the CdSe core causes the emission to be governed by the CdSe core resulting in a large apparent Stokes shift. Increasing the shell thickness also proved to be beneficial for the photostability of the particles. Despite the good efficiencies obtained using these giant CdSe/CdS core/shell NCs the large-scale deployment is severely limited. As these heavy metal containing compounds pose a substantial risk to our health and the environment[60]. This has motivated a worldwide search for heavy-metal-free alternatives.

One of the most promising candidates are the ternary I-III-VI materials[24,29]. Besides their lower inherent toxicity, facile synthesis and potential low production cost, they possess similar characteristics to the instrumental Cd- and Pb-chalcogenide NCs. Moreover, they show properties that are unmatched by their Cd and Pb containing analogues, like a large Stokes shift[6]. The most thoroughly investigated I-III-VI NC, and the materials of interest for this work, is $CuInS_2$ (CIS). Figure 9 gives a good impression of the great potential of CIS QDs for LSCs.

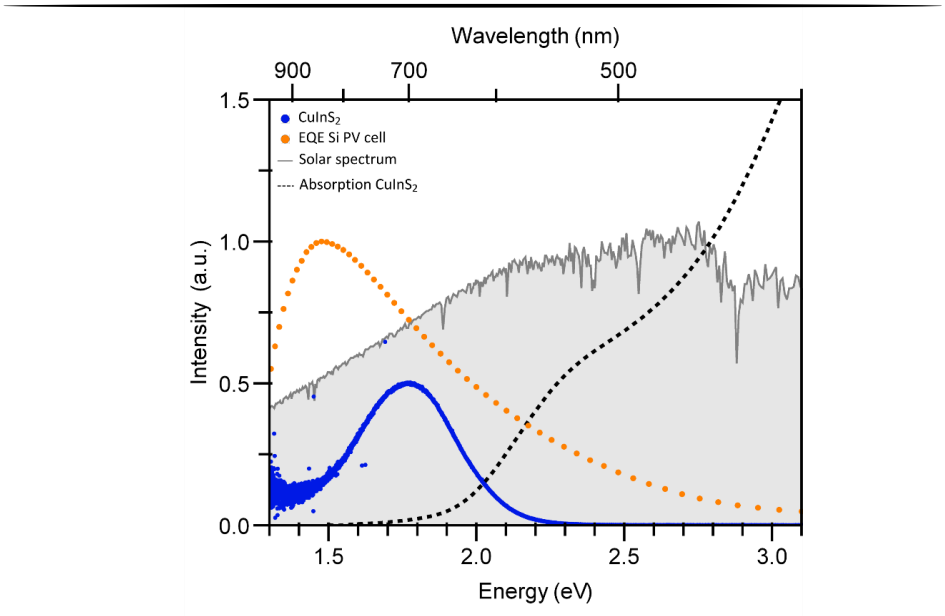

Figure 9 · Absorption and emission spectra CIS plotted with the solar spectrum and the quantum efficiency of a Si based PV cell. The emission CIS in the NIR of make these materials suitable fluorophores in combination with Si PVs. The CIS absorption spectrum also shows promising compatibility for LSC application as the material shows significant absorption on the high energy side of the solar spectrum.

2.3.2. Quantum dot-based light-emitting diodes

In the process of electroluminescence (EL) a material is excited by an electric current and emits light upon radiative recombination. A conventional LED consists of an anode, a hole transport layer (HTL), an emissive layer (EML), an electron transport layer (ETL) and a cathode[53,61]. QD-LEDs are typically structured in the same way where the QDs function as the electroluminescent material in the EML. The transport layers are designed in such a way to match the energy bands of the EML.

The tuneable and narrow emission bands of QDs make them very versatile materials for this application. On top of that their relatively easy processability and stability lead to great interest in the development of QD-LEDs when it was first prototyped in 1994[61]. As a result of almost three decades of research, a number of corporations and start-ups developing QD-LED displays for the large public[62,63]. However, similar to LSCs, most of the advanced QD-LED devices contain heavy metals, like Cd and Pb, severely limiting its incorporation in numerous applications. So, in order to keep on developing QD-LEDs, heavy metal free alternatives are required. Several alternatives show tunability over the visible spectrum with similar electronic band structures as CdSe, which means that they could function in previously designed and optimized CdSe-based devices[53]. The III-V class shows the greatest potential in substituting the II-VI compounds[64,65]. The most thoroughly investigated III-V material is InP.

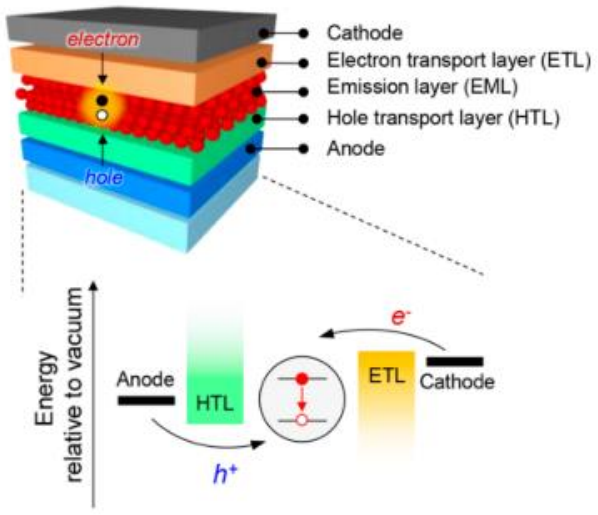

Figure 10· Schematic representation showing the different components of a QD-LED at the top. At the bottom the energy band diagram is displayed showing the charge carrier transport to the emissive layer wher they recombine radiatively. The figure was reproduced from ref. [32].

3. Reverse type-I InP quantum well NCs

In this section we investigate the potential of a relatively new route to synthesize InP NCs with tuneable PL covering the entire visible spectrum into the NIR. The new synthesis protocol relies on the formation of a spherical quantum well[66]. This core/shell/shell system comprises a core of a wide bandgap material encapsulated by, in our case InP shells, which in turn is overcoated by another even wider bandgap material to passivate the surface. In this way both charge carriers are localized in the first shell instead of the core, as for a type-I system, which is why spherical quantum well systems are also referred to as reverse type-I energy band alignments. By growing the InP shell layer by layer, accurate control over the polydispersity of the sample is gained provided monodisperse core NCs are used. In literature there are only few reports on this method[67,68]. Dennis et. al.[67] report PL activity over the entire visible range into the NIR[67]. Due to the little information found about this synthesis we set out to explore this method.

3.1. Synthesis ZnSe/InP core/shell NCs

For the core material we use ZnSe NCs because of its well-known synthesis, photoluminescence in the blue and relatively low polydispersity[69,70]. By growing InP shells around ZnSe NCs emitting in the blue we aim to develop materials that covers the entire visible range into the NIR by increasing the InP shell thickness. For the synthesis we followed the method described in ref. [71][70]. Figure 11 shows the absorption and emission spectra of ZnSe NCs. The absorption spectrum shows a clear peak corresponding to bandgap of 3.17eV. The emission peak is centred at 3.05eV giving a Stokes shift of 120meV. To control the size dispersion of the ZnSe/InP core/shell NCs, successive ion layer adsorption and reaction (SILAR) is used. For the cation precursor we use TBP-In and In-oleate and for the anion precursors we use $P(TMS)_3$. The TBP-In matches the reactivity of $P(TMS)_3$ while In-oleate is a more stable precursor. During the synthesis aliquots are taken to study the effects of precursors addition.

Upon addition of the first monolayer (ML) of InP, using the TBP-In and $P(TMS)_3$ precursors, the optoelectronic properties are immediately affected. Figure 12A shows a significant redshift of the first absorption features. However, upon increasing the amount of InP precursors added the

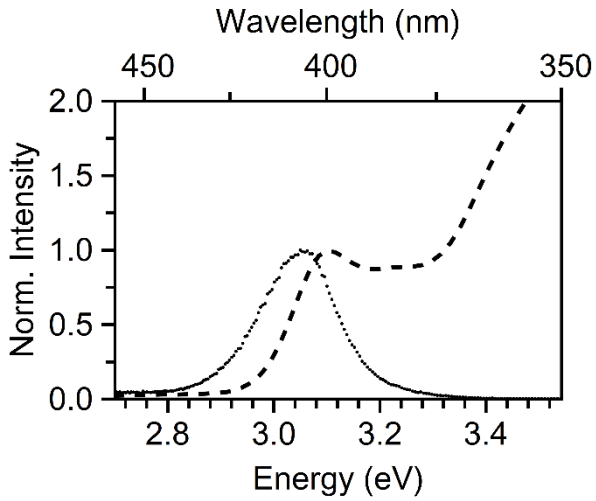

Figure 11 · The absorption and emission spectrum of ZnSe NCs. The absorption spectrum has a clear peak at 3.17eV representing the bandgap energy. The emission peak is centred at 3.05eV resulting in a Stokes shift of 120meV

absorption peak remains constant around 2.5 eV. Increasing the number of MLs gradually makes the absorption spectrum featureless, leading to a broad first energy transition peak. Initial addition of the InP precursors diminishes the PL band. Though only very weakly, after addition of the third ML an emission signal is around 1.5 eV. The changes in the absorption and emission properties are characteristic for the onset of a type-II energy level alignment[1,27,71]. Although undesirable, the formation of a type-II system suggests InP shells are grown around the ZnSe core NCs. This is checked by determining the particle increase using transmission electron microscopy (TEM). The TEM images, however, show no particles at all. This could indicate that the sample is not washed properly and is still full of organics, or that the NCs dissolve during the core/shell synthesis.

The ZnSe/InP core/shell NC synthesis using In-oleate as cation precursor appears to have similar problems. The absorption spectra are redshifted. The PL band of the ZnSe NCs is lost upon first addition of the InP precursors and, as for TBP-In, a weak PL signal in the NIR can be observed after addition of the sixth ML.

We hypothesize that due to the reactivity of both precursors InP nuclei form during the reaction. The initial red shift observed for the reaction using TBP-In and the weak PL signal after the addition of the third ML suggests the presence of an additional species of NCs. This explains the structure loss and redshift of the absorption spectra. To check this hypothesis, we add each precursor separately to the ZnSe core QDs under the same reaction conditions and take aliquots. $P(TMS)_3$ does not affect the ZnSe core QDs (figure 12C). TBP-In, however, seems to dissolve the ZnSe NCs (figure 12D). After four hours the reaction mixture turns brown and the absorption spectrum shows characteristics of Rayleigh scattering. To verify if InP NCs are formed we mix both precursors without the ZnSe cores (for both precursor couples). Mixing of the TBP-In with the $P(TMS)_3$ causes an immediate colour change, followed by crystallization of an precipitate. The absorption spectra show an exponential trend, characteristic for scattering (figure 12E). Based on these results we conclude that $P(TMS)_3$ and TBP-In are unsuitable precursors for InP shell growth. The same control experiment is performed for In-oleate. Figure 13F shows almost identical absorption spectra compared to figure 13B. We propose that the extra absorption feature at 2.6 eV indicates InP NC formation and the second feature represents the ZnSe NCs.

3.2. Conclusions

What set out to be an interesting exploration into a relatively new synthesis method of InP quantum well NCs, proved to be very challenging. For further research efforts one could look into the usage of different antisolvents improving the removal of organics in order to image the samples. Moreover, better balanced InP precursors in terms of reactivity towards the ZnSe cores and each other could facilitate the desired shell growth.

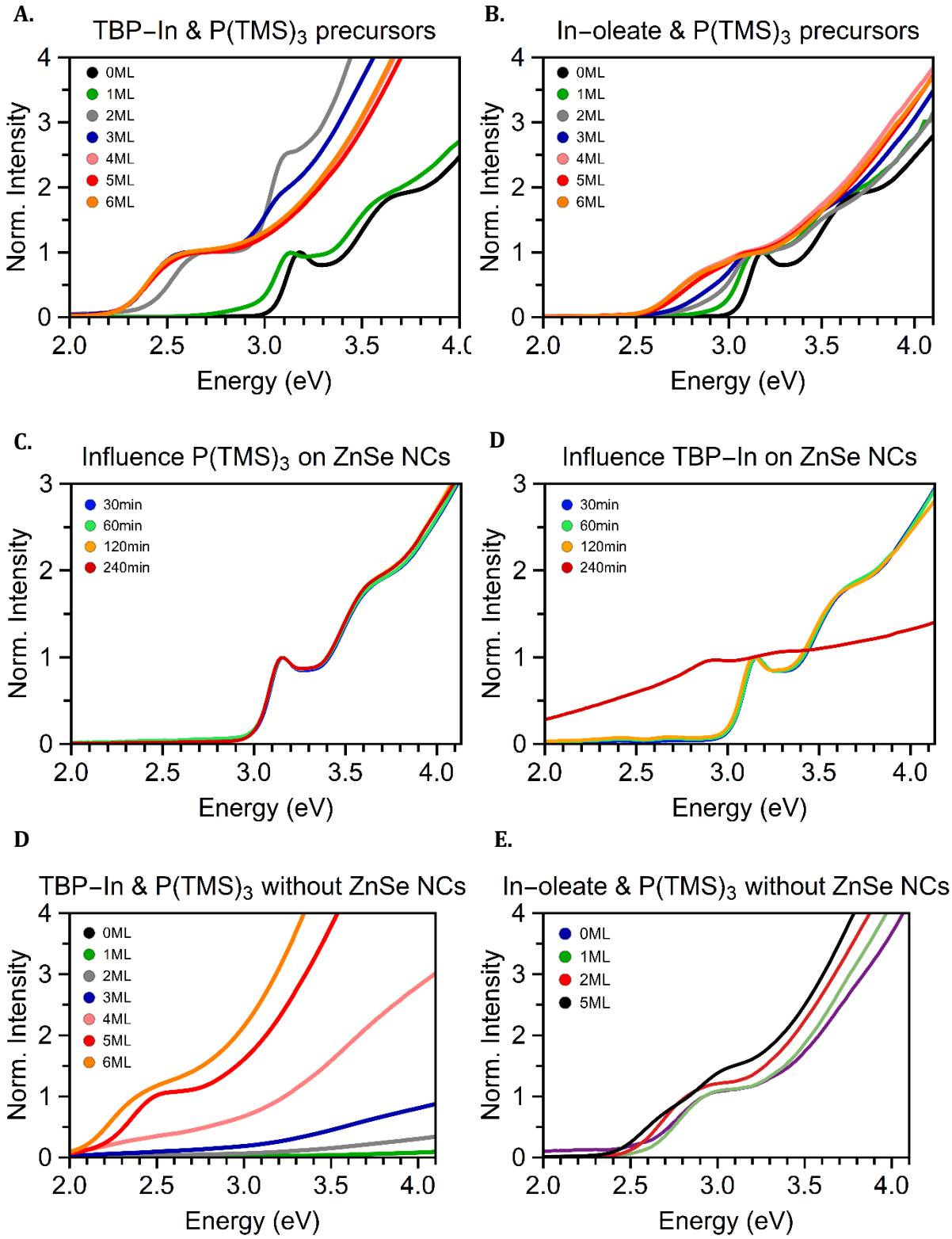

Figure 12 · A. Absorption spectra of the aliquots taken during the ZnSe/InP core/shell synthesis using TBP-In as a cation precursor. **B.** Absorption spectra of the aliquots taken during the ZnSe/InP core/shell synthesis using In-oleate as a cation precursor. **C.** Effect of $P(TMS)_3$ on ZnSe when mixed under the same reaction conditions as for the core/shell synthesis. **D.** Effect of TBP-In on ZnSe when mixed under the same reaction conditions as for the core/shell synthesis. **E.** Absorption spectra of the control experiment to check InP formation during the core/shell synthesis using TBP-In as a cation precursor. F. Absorption spectra of the control experiment to check InP formation during the core/shell synthesis using In-oleate as a cation precursor.

3.3. Methods

Chemicals. *Octadecene (ODE, Sigma Aldrich, 90%), oleic acid (OA, Sigma Aldrich, 90%), Trioctylphosphine(TOP, Fischer Scientific, 97%), Octadecylamine (ODA, Fluka, 90%), diethylzinc ($Zn(Et)_2$, Strem Chemicals, 98%), Selenium powder (Se, Alfa Aesar, 99.999%), Toluene (Sigma Aldrich, 99.8%), Acetone (VWR International bv, dried, max. 0.0075% H_2O), Hexane (Sigma Aldrich, 99.8%).*

ZnSe core synthesis. *First, the Zn-precursors, a Se-precursor and a solvent were prepared in a glovebox. A 0.4 M $Zn(Et)_2$ stock solution was made by dissolving 4 mmol $Zn(Et)_2$ in 10 mL ODE. The second cation precursor was prepared by adding 5.05 mL OA in a dropwise fashion to solution of 4 mmol $Zn(Et)_2$ and 4.95 mL ODE (4:1 OA:$Zn(Et)_2$). The Zn-oleate was allowed to react for 5 min at 300 ^{0}C. The anion precursor was prepared by dissolving 10 mmol Se powder in 10 mL TOP. For the solvent 4.4 g ODA was dissolved in 20 mL ODE and degassed for ~15 hs at 100 ^{0}C. For the synthesis 2.52 g of ODE-ODA solvent was heated to 290 ^{0}C inside a glovebox. At this temperature, under heavy stirring, 0.5 ml $Zn(Et)_2$ stock and 0.67 mL Se stock was quickly injected. The temperature dropped due to the injection and maintained at 270 ^{0}C. Five minutes after the injection, 1.5 mL Zn-oleate diluted with 3 mL ODE was manually added in dropwise fashion over the course of 20-25 min. The synthesis was stopped 10 min after the end of the Zn-oleate addition by removing the heating source. Unreacted precursors were removed using hexane/methanol extraction. The crude reaction mixture was mixed with anhydrous hexane and anhydrous methanol (1:4:2 volume ratio). The ZnSe QD containing top layer was removed and dispersed in an equal volume of methanol. The extraction steps were repeated 5 times before flocculating the QD by adding a antisolvent (anhydrous acetone) (1:6 volume ration). The precipitated QDs were isolated by centrifugation (2850 rpm, 12 min) and dispersed in anhydrous toluene.*

ZnSe/InP core/shell synthesis. *The 0.2 M TBP-In stock solution was prepared by dissolving 2 mmol $InCl_3$ in 10 mL TBP. A 0.2 M In-oleate stock solution was made by mixing 1 mmol $In(Ac)_3$ with 3 mmol OA and 12 mL ODE. The mixture was degassed for an hour at 120 ^{0}C, before raising the temperature to 160 ^{0}C under N_2 flow. The mixture was allowed to react for 2 hours before lowering the temperature again to 120 ^{0}C. Once at 120 ^{0}C the mixture was further degassed for ~15 hs. The highly reactive $P(TMS)_3$ was diluted in 5 mL ODE to obtain a 1M stock solution inside a glovebox. For the shell growth synthesis 100 nmol ZnSe cores were dried in a vacuum chamber and mixed with 2.7 mL ODE and 0.3 mL oleylamine. The solution was heated to 150 ^{0}C and, while stirring, the volume sufficient for one ML of In-precursor was added. 15 min after addition the volume required for one ML of P-precursor was added and the temperature was raised to 178 ^{0}C and maintained for one hour. After 60 min the temperature was lowered again to 150 ^{0}C and the previous two steps were repeated with adjusted volumes of In- and P-precursors for the subsequent MLs. Aliquots were taken 30 and 60 minutes after addition of the P-precursor. The reaction was stopped by removing the heating once the desired amount MLs were added.*

Steady state optical spectroscopy. *The core and core/shell samples for optical measurements were diluted in toluene and stored in cuvettes. Absorption spectra were recorded using a double-beam Perkin-Elmer Lambda 116 UV/vis spectrometer.*

4. Synthesis and characterisation of CIS NCs

In this chapter the synthesis and optical properties of CIS NCs is discussed. As discussed in chapter 2.2.1. the NCs are synthesized using the heating up method. Preliminary absorption and (time resolved) emission spectroscopy measurements confirm the synthesis CIS core, CIS/ZnS and CIS/CdS core/shell NCs (chapter 4.1.). In chapter 4.2. the size, shape and crystal structure of the CIS NCs is determined using electron microscopy, Small- and Wide-angle X-ray Scattering. Chapter 4.3. reports on the scaled-up synthesis and the effect of thick CdS shells on the absorption cross section and PLQY.

4.1. CIS NCs synthesis and optoelectronic properties

CIS NCs are synthesized following the heating up method. Through slow injection ZnS and CdS shells are grown around the CIS core NCs as described in ref. [29][28]. Figure 13 shows the featureless absorption spectrum, broad emission band, large global Stokes shift and long radiative lifetime characteristic for CIS NCs. The bandgap energy can reliably be determined by locating the first minimum of the second derivative of the absorption spectrum (black, dashed-dotted line) (figure 13A)[72]. The bandgap of the CIS core, CIS/ZnS and CIS/CdS core/shell NCs are 2.27eV, 2.29eV, 2.19 eV respectively. The PL bands are centred at 1.73eV, 1.83eV and 1.76 eV resulting in a global Stokes shift of 540meV, 460meV and 430meV for CIS core, CIS/ZnS and CIS/CdS core/shell NCs respectively. The beneficial effects of shell growth on the quantum efficiency is obvious when looking at the significant increase of the PL intensity. For CIS/ZnS core/shell NCs this increase is by a factor of 5 and even by a factor of 11 for CIS/CdS core/shell NCs. The improved optoelectronic properties due to surface passivation immediately follow from the PL decay spectra as well (figure 13B). All samples decay multi-exponentially, so the radiative lifetimes are approximated by determining at what delay time the excited state has decayed 1/e (21ns, 142ns, and 322ns for CIS core, CIS/ZnS and CIS/CdS core/shell NCs respectively).

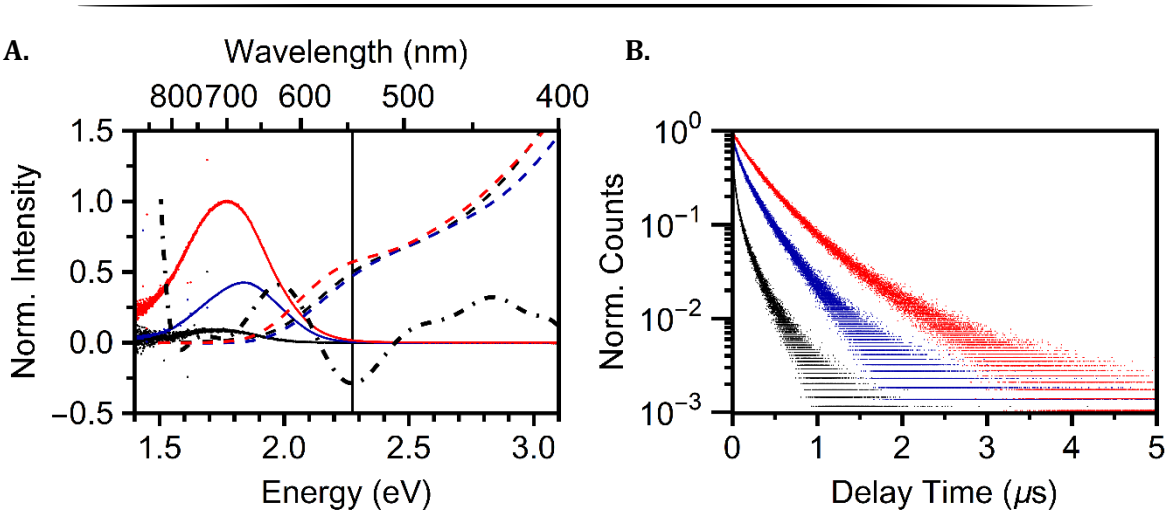

Figure 13 · A. Absorption and emission spectra CIS core (black), CIS/ZnS (blue) and CIS/CdS (red) core/shell NCs. From the absorption spectra the bandgap of the samples is determined by locating the first minimum of the second derivative of the absorption spectrum (black dash-dotted). Surface passivation through shell growth significantly increases the PL intensity (increase by a factor 5 and 11 for CIS/ZnS and CIS/CdS respectively). **B.** The decay curves of CIS cores (black), CIS/ZnS (blue) and CIS/CdS (red) core/shell NCs, the radiative lifetimes are approximated at 21ns, 142ns and 322ns respectively.

For CIS/ZnS core/shell NCs a blueshift of the PL band is observed. In literature this blueshift is ascribed to different explanations but most likely arises due to alloying[6,73–75]. As the literature strongly suggests copper centres play a key role in the exciton recombination pathway in CIS NCs. The exchange of Cu^+ with Zn^+ ions is therefore undesirable when studying the recombination dynamics of CIS NCs. CIS/CdS core/shell NCs do not show this behaviour due to the large lattice mismatch and are therefore more likely to represent the intrinsic properties of CIS NCs.

The NC size can be determined based on the absorption spectrum provided a sizing curve has been designed for the material. The size-dependence of the optical properties of NCs allows the construction of empirical sizing curves correlating the first energy transition in the absorption spectrum to the NC size[72]. The authors of ref [73][72] designed a sizing curve for chalcopyrite CIS NCs using TEM data from various sources. A bandgap of 2.27 eV corresponds to a NC diameter of 2.29nm assuming spherical NCs. For the core/shell NCs, both the core and shell contribute to the absorption cross section of the compound, so a different sizing curve is required[76]. In addition to the sizing curve, the intrinsic absorption coefficient (μ_i) of the material needs to be calculated. μ_i is an intrinsic property that states the attenuation of light as it travels through the composite in a given solvent for a specific wavelength. To calculate this quantity, one must consider the interaction of light with the material assuming a particle shape. So, one could argue the NC size is more accurately determined using different techniques like electron microscopy or X-ray diffraction techniques.

4.2. Size, shape and crystal structure characterisation

In this section different characterisation techniques are used to determine the NCs size, shape and crystal structure. The NCs are imaged using High-Angle Annular Dark Field Scanning Transmission Electron Microscopy (HAADF-STEM). The CIS NCs prove to scatter the electron beam poorly resulting in low contrast STEM images. For this reason, the NC size cannot be determined accurately, however, clear triangles can be distinguished indicating a tetrahedral shape. The crystalline domain and radius of gyration is estimated by analysing Small- and Wide-Angle X-ray Scattering (SAXS and WAXS) data. Both the crystalline domain and the radius of gyration can be related to a specific edge length of a tetrahedron, thus determining the NC size.

4.2.1. Transmission electron microscopy

The CIS core and CIS/CdS core/shell NCs are imaged using a Philips Tecnai 20feg microscope. Figure 14 presents an HAADF-STEM image of CIS/CdS core/shell NCs. Clear triangles are observed verifying the tetrahedral shape. As the contrast of the image is very weak the NC size is difficult to determine. The low contrast is a consequence of the relatively light atoms in CIS NCs. Atoms with a low atomic number and thus a low electron density, only weakly scatter the electron

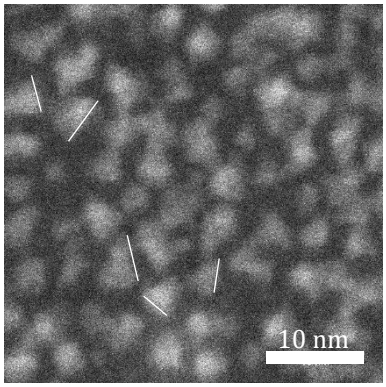

Figure 3 · HAADF-STEM image of CIS/CdS core/shell NCs obtained using a Philips Tecnai 20feg electron microscope. The triangles verify the tetragonal crystal structure. The edge lengths of the highlighted triangles were manually determined (3.8 nm on average).

beam thus lowering the contrast of the NCs with respect to the grids[77]. Due to this the and the smaller size the CIS core NCs could not be visualised using this microscope. The edge lengths of the highlighted triangles are manually determined resulting in an edge length of …nm. To get a more accurate idea of the particle size X-ray diffraction experiments are performed.

4.2.2. Small- and Wide-Angle X-ray Scattering

At the Soleil synchrotron in Paris, France the SAXS and WAXS patterns are acquired using a SWING 16 keV X-ray beam (figure 15A). SAXS and WAXS data is often represented by plotting the scattering intensity as a function of the scattering vector q:

$$q = \frac{2\pi}{d} \tag{6}$$

with d the lattice spacing, i.e. the distance between the crystal planes. Figure 15B plots the WAXS data together with a reference diffraction pattern of chalcopyrite CIS NCs, from ref [79][78]. A perfect crystalline material with infinite periodicity gives rise to infinitely sharp scattering peaks[79]. However, in practice the material is never perfectly crystalline and, especially for NCs, the periodicity is finite, causing peak broadening in the diffraction pattern. In 1918, the German physicist Paul Scherrer related the width of the diffraction peaks to the mean size of the crystalline domain, τ, of a crystal[80]:

$$\tau = \frac{2\pi \mathrm{K}}{\beta} \tag{7}$$

with K the Scherrer constant and β the integral breath. The value of K is dependent of the Miller indices of the crystal plane and the crystal geometry. For tetrahedral shapes K is approximately 1[79]. The integral breath is defined as the total area under the diffraction maximum divided by the peak intensity. As K is determined by the Miller indices of a crystal plane, only the integral breath of a peak caused by a single crystal plane can be used. The reference figure shows that none of the peaks in the WAXS data arise from a single crystal plane. The peak at 4.5q, however, primarily arises from the (400) plane. So, by fitting a Gaussian through this peak, β is estimated. The crystalline domain is determined using Eq. 7 (τ = 2.7 nm). τ can be related to an edge length of different crystal geometries[79]. As such the edge length of tetragonal CIS NCs is calculated; 5.5nm.

Another way to approximate the NC size is by calculating the radius of gyration of a particle. This is done using Guinier analysis of the SAXS data. In a Guinier plot the natural logarithm of the scattering intensity is plotted as a function of q^2. In the Guinier regime ($<1\ q^2$), the slope of this plot can be fitted with a linear function. The slope of this straight line is indicative for the radius of gyration[81]. Figure 15C shows the Guinier plot of CIS NCs. The radius of gyration was determined at 1.2 nm. A radius of gyration of 1.2 nm for tetrahedrons relates to an edge length of 4.3 nm.

The edge lengths obtained with SAXS and WAXS are considerably larger than the lengths obtained from HAADF-STEM. In literature a similar trend can be found for small particles as HAADF-STEM tends to underestimate the actual NCs size due to weak electron contrast[77].

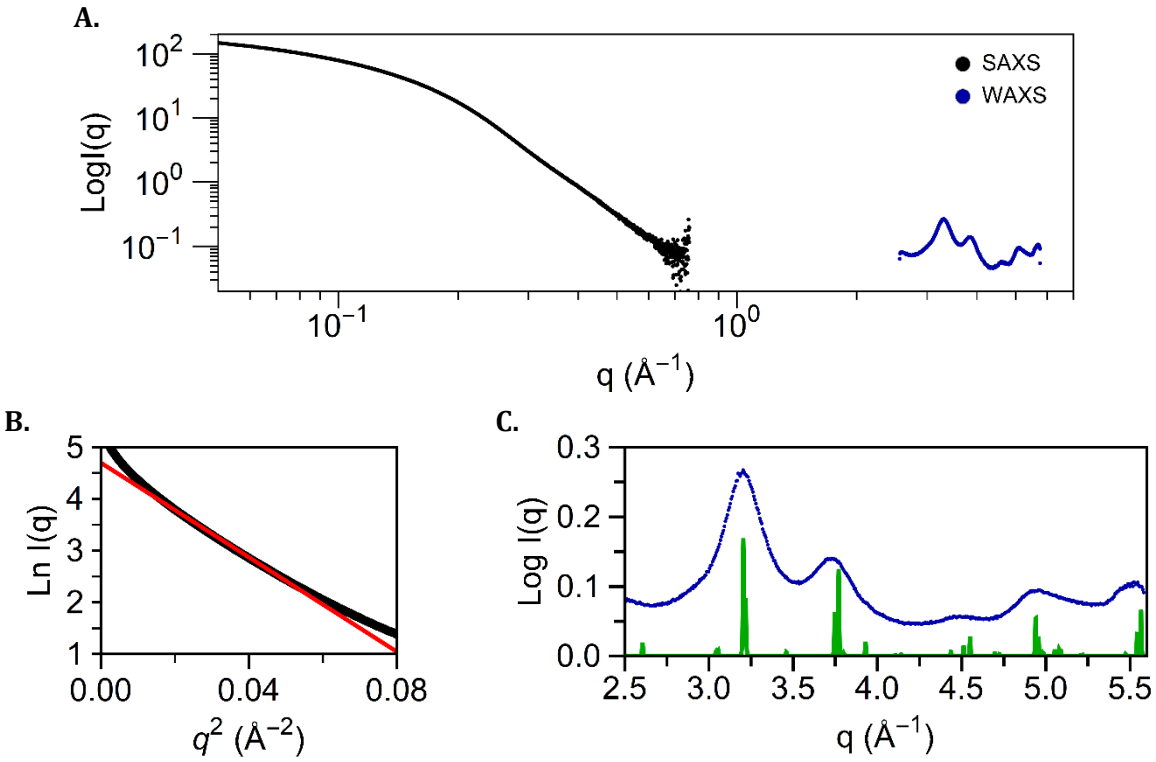

Figure 4 · A. The scattering intensity of the SAXS (black) and WAXS (blue) data plotted as a function of q. **B.** The Guinier showing the natural logarithm of the scattering intensity as a function of q^2. From the slope of the straight line fitted through the SAXS data (red) in the Guinier regime the radius of gyration can be calculated. **C.** The scattering intensity of the WAXS data (blue) as a function of q, plotted with a reference spectrum of chalcopyrite CIS NCs (green). The Miller indices of the crystal planes are labelled next to the reference peaks.

4.3. Scaled-up synthesis and thick shell CIS/CdS core shell synthesis

In ref [31] the scaled-up synthesis of CIS NCs is described by increasing the amount of Cu- and In-precursors while keeping the solvent volume and S-precursor constant. For the shell overgrowth procedure, we linearly increase the Cd- and S-precursors volume added to obtain the same NC core to shell precursor ratio. To prevent the nucleation of CdS NCs, the injection rate of the shell precursors is reduced so that the concentration of added precursor per time unit is the same as for the regular synthesis method. Figure 16 shows the emission and absorption spectra of the regular core/shell synthesis and the scaled-up method. The relative PLQY is decreased by 15% for the scaled-up method relative to the normal core/shell methods but is still significantly higher than for CIS core NCs. The PL decay curves are very similar, with a slightly slower decay rate for the scaled-up synthesis. Besides the scale of the synthesis the samples also differ in CIS core NCs size. This probably explains the difference in decay rate as the cores show a similar trend in decay rates.

As the reaction time is increased for the scaled-up synthesis, we attribute the PL redshift to the growth of thicker CdS shells. The absorption cross section, σ, of a material increases with the material volume as follows:

$$\sigma = V_{NC}\mu_i \tag{10}$$

with V_{NC} the NC volume and μ_i the intrinsic absorption coefficient. The absorbance of the scaled-up synthesis is increased almost over the entire spectrum, indicating a larger NC volume. The

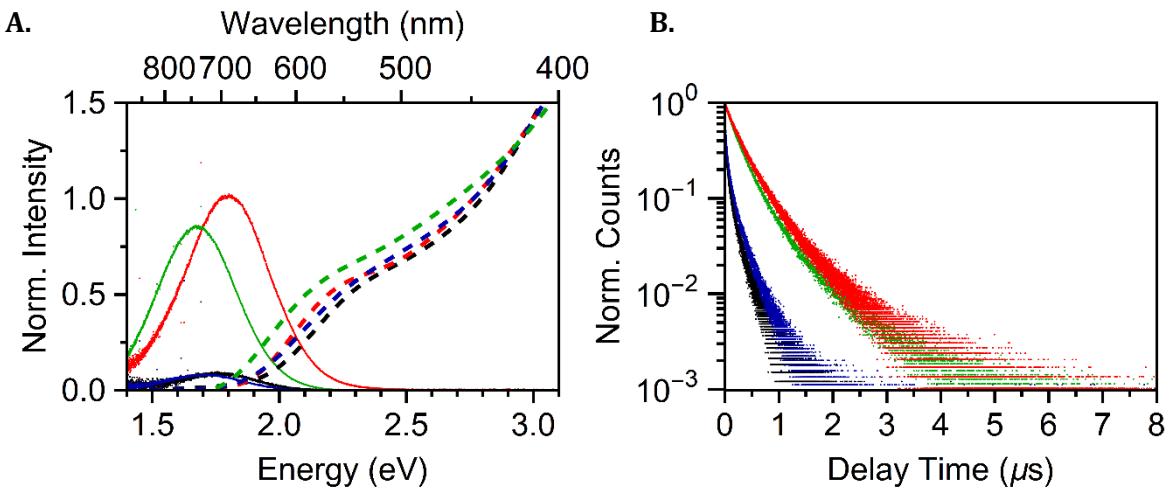

Figure 16 · A. The absorption and emission spectra of both CIS core NCs used for the regular and scaled up CIS/CdS core/shell synthesis are very similar. The PLQY of the regular CIS/CdS core/shell NCs synthesis (red) is considerably higher for the scaled-up synthesis (green). **B.** The CIS core NCs for the regular synthesis (black) has a slightly faster radiative decay rate compared to the CIS core NCs used for the scaled-up core/shell synthesis (blue). The increased scale does not seem to affect the radiative decay rate much.

increased absorption cross section can improve the detection of the NC in sensitive spectroscopy techniques like singe particle spectroscopy. So, we further explored the effect of thick CdS shells on the optoelectronic properties of the material.

Thick CdS shell were grown by increasing the shell precursor concentration and add them at a decreased rate, again to prevent CdS NC nucleation. Figure 17A shows the absorption and emission spectra of the normal, scaled up and thick shell CIS/CdS core/shell synthesis. The large redshift of the PL band of the thick core/shell sample supports the hypothesis that the redshift for the scaled-up synthesis is due to an increase of the shell thickness. The increase of the CdS shell and thus the increase of the absorption cross section is, however, accompanied by a decrease of the PLQY. We attribute this decrease to two phenomena. First, the interfacial strain induced by lattice mismatch between the core and shell material becomes too high, hence lowering the PLQY[66]. Secondly, upon increasing the shell thickness the energy band offset at the core/shell heterointerface decreases, allowing the core electron to delocalize into the CdS shell. In this way the Type-I energy band alignment is transformed into a Type-I$^{1/2}$. Delocalization of the core electron reduces the e-h overlap, increasing the non-radiative decay rate (figure 17B)[27]. From Eq. 5 it can easily be derived that an increase in the non-radiative decay rate causes the quantum efficiency to drop. It is therefore important to find a balance between an increased absorption cross section and the loss of the PLQY for CIS/CdS core/shell NCs for an adequate signal to noise ratio.

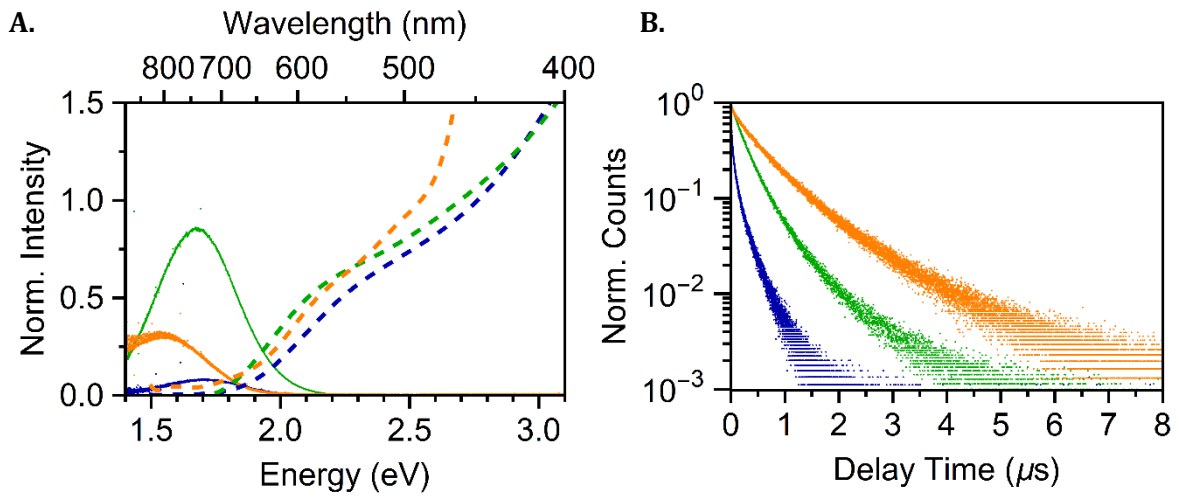

Figure 17 · A. The absorption and emission spectra of the CIS core (blue), scaled-up CIS/CdS core/shell (green) and the CIS/CdS core/thick shell NCs (orange). The PL band is significantly redshifted compared to the PL band of the scaled-up core/shell sample. **B.** The radiative decay curve of the thick CdS shell sample is significantly longer compared to the scaled-up synthesis. We attribute the redshift observed for the PL peak and the increased lifetime to the formation of a Type-$I^{1/2}$ energy band alignment.

4.4. Conclusions

The characteristic photophysical properties of CIS NCs (featureless absorption spectrum, broad PL band, long lived radiative lifetimes and large global Stokes shift) confirm the synthesis of CIS NCs and the significant increase of the PLQY due to surface passivation indicate successful shell growth of ZnS and CdS shell. Using HAADF-STEM the tetragonal crystal shape of CIS NCs is confirmed and an average size of 4.9 nm is calculated from the SAXS and WAXS data. The scale of the synthesis does not seem to affect the optoelectronic properties of CIS/CdS core/shell NCs much. The redshift of and decreased intensity of the PL band is attributed to delocalization of the core electrons into the CdS shell due to formation of Type-$I^{1/2}$ energy band alignment. To study the nature of the broad PL band (chapter 5) and the exciton recombination pathway (chapter 6) in CIS NCs a wide range of (sensitive) spectroscopy techniques are used. In order to perform these experiments with a single NCs sample we decided to use the scaled-up CIS/CdS core/shell NCs. As the CdS shell enhances the optoelectronic properties of CIS NCs while conserving the CIS (nano)crystal structure.

4.3. Methods

Chemicals. *Copper (I) iodide (CuI, Sigma Aldrich, 98%), Indium (III) acetate ($In(Ac)_3$, Sigma Aldrich, 99.99%), 1-dodecanethiol (DDT, Sigma Aldrich, ≥98%), Trioctylphosphine (TOP, Fischer Scientific), Zinc (II) stearate (Sigma Aldrich, 10-12% Zn basis), Cadmium (II) oxide (Sigma Aldrich, 99.5%), Oleic Acid (OA, Sigma Aldrich, 90%), 1-octadecene (ODE, Sigma Aldrich, tech. 90%), Sulphur (Sigma Aldrich, 99.98%), Toluene (Sigma Aldrich, 99.8%), Acetone (VWR International bv, dried, max. 0.0075% H_2O). ODE was degassed for 2 hours at 110 ^{0}C before usage.*

CIS NC synthesis. *For a typical CIS synthesis, 1 mmol indium acetate ($In(Ac)_3$) was mixed with 1 mmol copper iodide (CuI) and 5 mL 1-dodecanethiol (DDT). The rection mixture was degassed for 10 min and flushed with N_2 three times. Under N_2 atmosphere the reaction flask was heated to 100 ^{0}C for 30 min until a clear solution was formed. The temperature was lowered again to 60-70 ^{0}C and degassed for another 30 minutes to remove all acetates and iodide. The above to steps were repeated until no bubbles were observed when the flask was put under vacuum. The temperature was then (rapidly) raised to 230 ^{0}C. A gradual colour change from colourless to red and eventually black was observed when increasing the temperature. Once at 230 ^{0}C the CIS cores were allowed to grow for 5 minutes before quenching the reaction by removing the heat source and cooling the flask with compressed air. For shell growth the crude reaction mixture is required, if the bare cores*

are the desired product, they can be isolated by flocculating them using acetone as an anti-solvent and centrifugation. The supernatant was discarded, and the precipitated cores were dispersed in toluene. ***For the scaled-up core synthesis*** *the same steps were followed as described above, only using 3 mmol $In(Ac)_3$ and 3 mmol CuI. The same volume of DDT was used.*

CIS/ZnS and CIS/CdS core/shell NC synthesis*. For the overcoating procedure 1 mL of the crude CIS reaction mixture was diluted with 4 mL ODE and degassed for 5 minutes. The ZnS (CdS) shells were grown by dropwise injection of the Zn- (Cd-) and S-precursors. The Zn stock was prepared by dissolving 2 mmol zinc stearate in 20 mL ODE and degassing it for ~12 hs at room temperature. The Cd-oleate stock solution was similarly prepared by dissolving 3 mmol of cadmium oxide (CdO) in 3.9 mmol OA (1:4 CdO:OA) and 3.9 mL ODE. This mixture was then degassed for an hour at 80 ^{0}C before raising the temperature to 280 ^{0}C under N_2 atmosphere. Once all was dissolved and a clear solution was observed the temperature was lowered again to 110 ^{0}C and degassed for ~12 hs. The S-precursor was prepared by dissolving 4 mmol S in 4 mL trioctylphosphine (TOP) inside a glovebox. For the shell growth 1 mL Cd-oleate stock solution (or 4 mL Zn stock) was mixed with 400 µL S-precursor and 4 mL ODE inside a syringe. The precursors were injected to 1 mL crude CIS reaction mixture diluted with 4 mL ODE at 210 ^{0}C over the course of 20 minutes using a syringe pump. Once everything was injected the sample was annealed for 20 more minutes, after which the reaction was stopped by removing the heating source and cooling with compressed air. The core/shell sample were isolated following the same washing procedure as for the CIS cores.*

Scaled-up CIS/CdS core/shell synthesis. *For the scaled-up CIS/CdS core/shell NC synthesis concentration of the cation and anion precursors was doubled (2M S-TOP stock and 0.58M Cd-oleate stock solution). 3.6 mmol sulfer dissolved in TOP(2M), 3.6 mmol Cd-oleate (0.58M) and 12mL ODE were added to 9x the concentration of CIS NCs diluted in 36 mL of ODE. The injection rate was designed to match the amount of precursors added to the reaction volume per unit of time as for the regular synthesis (~0.6mL per minute) at the same temperature as for the regular synthesis.*

Thick shell CIS/CdS core/shell NC synthesis. *For the CIS/CdS core/thick shell synthesis 1.2 mL TOP-S (1M), 3mL Cd-oleate (0.38M) and 12mL ODE were added to 1mL crude CIS NCs obtained from a regular scale synthesis diluted in 4 mL ODE. The precursors were added over the course of 1h at similar temperatures as for the regular synthesis.*

SAXS/WAXS crystallography. *At the Soleil swing beamline CIS core NCs were analysed in a capillary using a SWING beamline with a 16 keV X-ray beam.*

Steady state optical spectroscopy. *The core and core/shell samples for optical measurements were diluted in toluene and stored in cuvettes. Absorption spectra were recorded using a double-beam Perkin-Elmer Lambda 116 UV/vis spectrometer. Emission spectra were measured on a simple CCD camera using a 395 nm LED as excitation source.*

Time-resolved PL spectroscopy. *The core and core/shell samples for time resolved PL spectroscopy were diluted with toluene and transferred in cuvettes. PL decay curves were obtained by time-correlated single-photon counting on a Hamamatsu photosensor module H1072001. A pulsed diode laser (EPL-445 Edinburgh Instruments, 55 ps pulse width, 200 kHz repetition rate) was used as excitation source.*

Electron microscopy. *The HAADF-STEM images were acquired using a Philips Tecnai 20feg electron microscope. Measurements were performed in high-angle annular dark field scanning transmission electron microscopy mode, with a current of 700 pA. Detection in this mode was done using a Fischione Instruments HAADF detector. Samples were prepared by drop-casting a NC solution in toluene on a carbon-coated gold grid.*

5. Photoluminescence line broadening of $CuInS_2$ NCs

In this section the nature of the broad PL signal observed for CIS NCs is discussed. As mentioned in the theory, line broadening can arise due to sample specific inhomogeneities, or due to effects native to the material, also known as homogeneous effects. To study the contribution of these effects, various ensemble spectroscopy techniques (PL excitation spectroscopy, temperature-dependent spectroscopy and time resolved PL spectroscopy) and single particle spectroscopy are used. As discussed in the previous chapter we used CIS/CdS core/shell NCs for these measurements because of their increased PL QY and stability and close resemblance to CIS core NCs.

5.1. Photoluminescence excitation spectroscopy

In photoluminescence excitation (PLE) spectroscopy the PL intensity of a sample is recorded at a fixed detection wavelength, while varying the excitation wavelength. By setting the detection wavelength on the tail on the blue side of the emission band only the PL of smaller particles in the sample will be detected[82]. As such the PL of a limited selection of emitters within the sample is recorded, allowing the assessment of the homogeneity of the sample. Increasing the detection wavelength causes a larger subset of the sample to be detected. The sum of the PL of different sized particles is detected, smearing out the recorded PLE features. In figure 18 a distinct peak, centred at 2.4 eV, in the PLE spectrum is observed when setting the detection wavelength in the far end of the emission tail. The FWHM of the lowest energy excitation band is reduced to 212 meV, which is significantly narrower than for the ensemble PL band. Increasing the detection wavelength smears out the PLE feature. The excitation spectrum recorded by setting the detection wavelength closer to the centre of the PL band (green), closely resembles the steady state absorption spectrum (black, dashed). This is a common feature for PLE spectroscopy as the

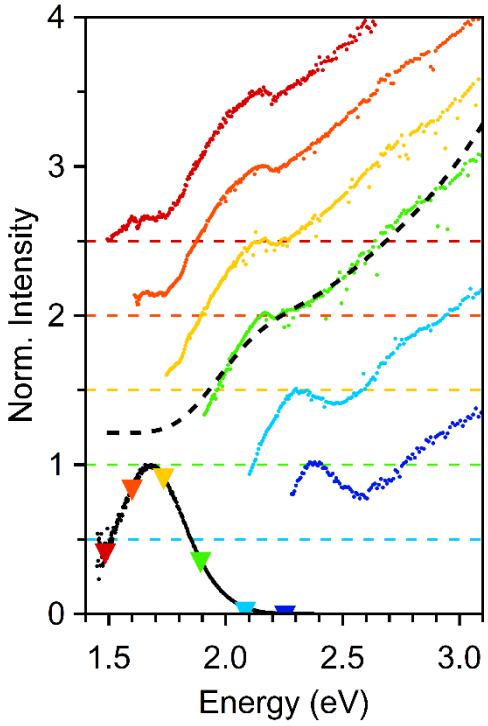

Figure 18 · PLE spectra of CIS/CdS core/shell NCs (coloured) measured by setting the detection wavelength at fixed wavelengths covering the entire PL band (black). The increase of the FWHM of the excitation peak upon increasing the detection wavelength indicates a considerable size dispersion in the sample.

spectrum arises from the emission of a larger subset of absorbers in the sample. The reduction of the FWHM for the first PLE spectrum (dark blue) compared to the ensemble PL band, in combination with the structure loss when increasing the detection wavelength, indicates a considerable size dispersion of the sample.

5.2. Temperature dependent spectroscopy

At cryogenic temperatures (<60 K) homogeneous broadening due to electron-phonon coupling is supressed, because the phonon states are decreasingly occupied with decreasing temperatures[83]. Consequently, at these low temperatures the PL broadening is dominated by inhomogeneous effects. In cryogenic experiments an increased lifetime is generally observed due to the existence of so called dark and bright states. In early theoretical work, by Efros et. al., CdSe exciton states were shown to be degenerate[20]. Following the electric-dipole approximation radiative recombination from the lower lying exciton states, or dark states, is forbidden[84]. Recent work by Knowles et al. hypothesizes that Cu^{+} centres play a key role in the bright and dark states of CIS NCs[38]. They propose that upon photoexcitation the hole localizes on a Cu^{+} ion forming paramagnetic Cu^{2+} (d^9 configuration). In this model there are two spins to be considered, the spin of the delocalized excited electron in the CB and the spin of the unpaired electron at the Cu^{2+} site (figure 18A). The orientation of these spins distinguishes to states: the singlet and triplet state. Radiative recombination from the triplet state is forbidden because of the spin selection rule ($\Delta S=0$) making the triplet state the dark state.

Figure 18B shows the decay curves of CIS/CdS core/shell NCs measured at cryogenic temperatures. At the boiling point of helium, the decay curve is almost a straight linear, indicating the primarily occupation of the forbidden triplet state. Increasing the temperature increases the population of the allowed singlet states thus decreasing the radiative lifetime which is in line with the literature[38].

The PL band of CIS/CdS core/shell NCs is temperature independent (figure 19A). The FWHM and peak position do not change upon increasing the temperature from 4 K to room temperature. Strongly supporting the inhomogeneous nature of the PL line broadening observed in the PLE experiments. Around the melting point of the solvent (ODE) a shift of the PL maximum is observed (figure 19B). This shift is understandable considering the environment around the luminescent material changes completely. At elevated temperatures the PL maximum redshifts. At high

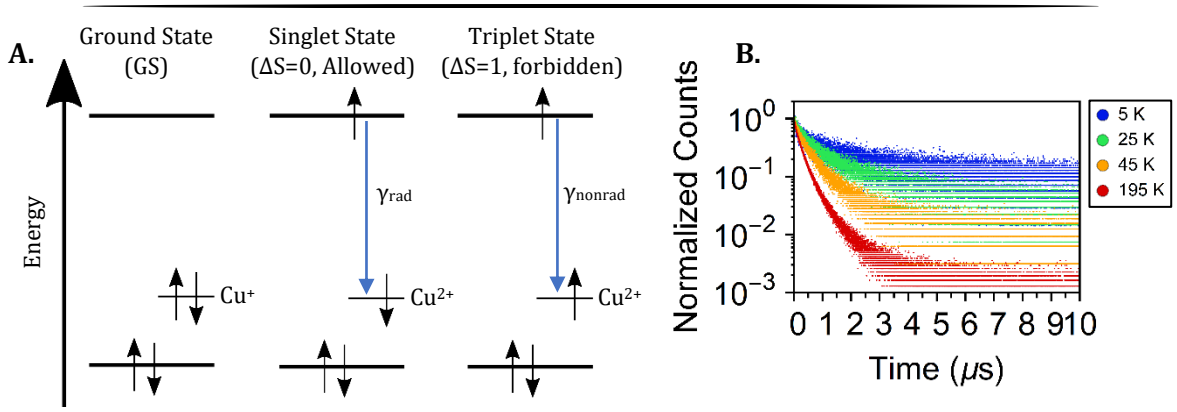

Figure 5 · A. Energy band diagram showing the ground state of CIS and the two excited states depending on the spin orientation at the Cu^{2+} centres. For the singlet state recombination is spin allowed hence this state is the bright state. The triplet state is a dark state as recombination of the exciton is spin forbidden. **B.** The PL decay curve of CIS/CdS core/shell NCs at low temperatures. Occupation of the lower energy triplet state causes extremely long-lived lifetimes at 5K. Increasing the temperature causes the bright state to become increasingly occupied increasing the radiative decay rate.

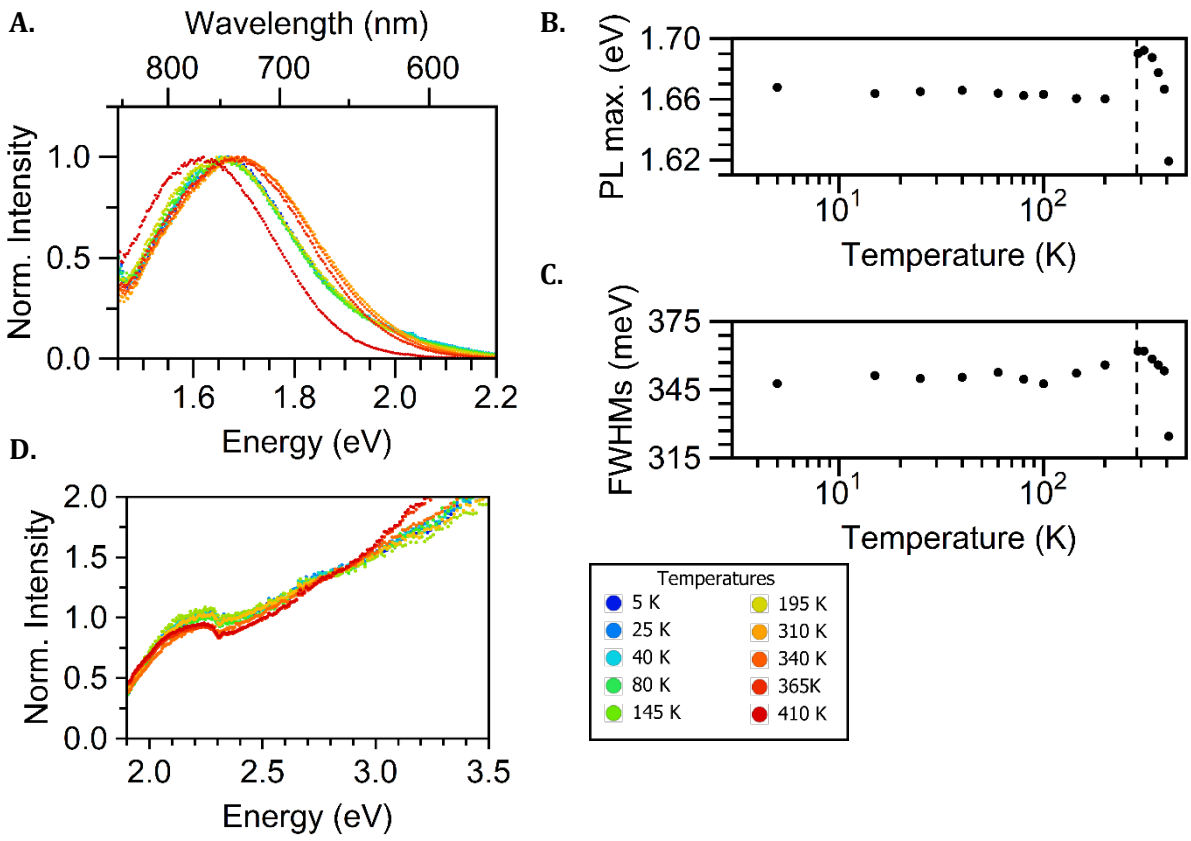

Figure 6 · A. Emission spectra recorded at different temperatures. **B.** The PL peak position plotted as a function of temperature. The constant peak position upon increasing the temperature from 4K to 195 K shows that the PL is temperature independent. At the melting point of the solvent (black dashed) the maximum shifts as the environment of the material changes. The redshift of the peak above RT are attributed to thermal quenching of smaller carriers. **C.** The FWHM plotted as function of temperature. The constant FWHM also indicates the temperature independency of CIS NCs. Above RT the narrowing of the PL band is also explained by thermal quenching of smaller NCs. **D.** The PLE spectra are unaffected by the changing temperatures, supporting the temperature independency of CIS NCs.

temperatures smaller particles can be quenched leaving the larger emitters to be observed and thus red shifting the PL band. The thermal quenching also explains the decrease of the FWHMs observed at these temperatures (figure 19C). As the PL is temperature-independent, the PLE spectra remain unaffected by temperature as well (figure 19D). The temperature-independence of the PL band when cooling the sample to cryogenic temperatures, supports the hypothesis that the sample is polydisperse. Moreover, the thermal quenching observed at elevated temperatures suggests the presence of different size population in the sample. These observations strongly indicate that the broad PL band observed for the ensemble is not necessarily native to the material.

5.3. Time resolved emission spectroscopy

TRES records the decay curves at incremental wavelengths over the entire emission band, resulting in a collection of emission spectra over time. Figure 20 plots the position of the emission peak over time. This plot shows a redshift of the emission spectra over time. We attribute this redshift, as the previous results also suggest, to polydispersity in the sample as well. Eq. 2 predicts a rough trend that the radiative lifetime increases with increasing emission wavelength. The PL peak will therefore redshift over time for a polydisperse sample. However, based on Eq. 2 this

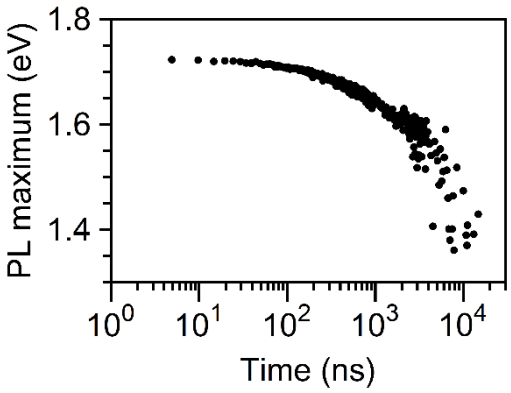

Figure 20 · Time-resolved PL spectroscopy shows the peak position of the PL band over time. Over time the emission peak redshifts. The redshift is explained due to polydispersity of the sample.

redshift should be linear. In literature deviation from this trend is generally observed as well, and is attributed to variations in the pre-factor C and the density of optical states ρ[22].

5.4. Single particle spectroscopy

So far, the nature of the PL bandwidth is assessed considering the ensemble. In this section the optoelectronic properties of single CIS/CdS core/shell NCs are studied. At the single particle level all ensemble effects are eliminated. Figure 21A shows the PL spectra of the ensemble and four single particles. The single NC spectra are significantly narrower with an average FWHM of ~210meV (figure 21B). This is an average reduction of the bandwidth by 52% with respect to the ensemble. The FWHM does not seem to be dependent of the particle size. The reduction of the

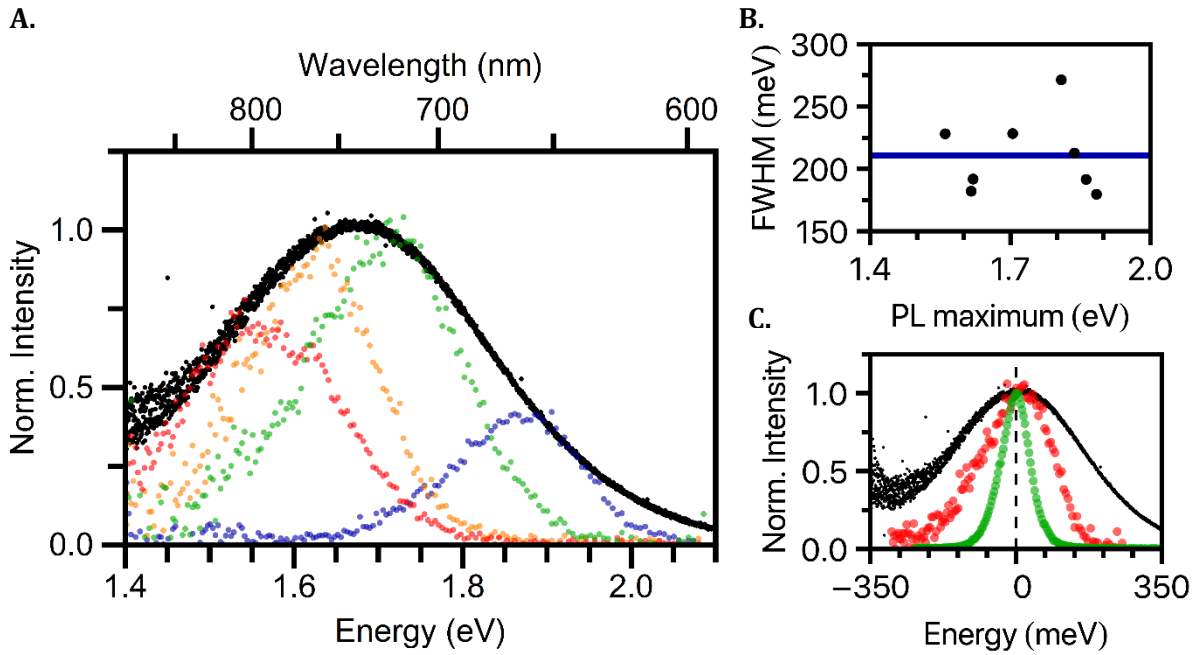

Figure 21 · A. Emission spectra of single CIS/CdS NCs (coloured) plotted with the ensemble PL spectrum (black) of the corresponding sample. Significant reduction of the FWHM is observed for the single NC spectra. **B.** The FWHM plotted as a function of the PL peak position. No trend arises when relating the FWHM to the PL peak position. **C.** An overlay plot of the PL spectra of the CIS/CdS core/shell NC ensemble (black), a single CIS/CdS core/shell NC with a FWHM resembling the average (red) and the CdSe/CdS core/shell NCs ensemble (green). The single particle spectrum is reduced by a factor of 0.52 compared to the ensemble band, but still almost a factor 3 wider than observed for CdSe/CdS core/shell NCs.

bandwidth on a single particle level substantiates the claim that the broad PL signal is due to polydispersity in the sample. However, the PL linewidth of single CIS/CdS core/shell NCs is still much broader than observed for the ensemble of II-IV compounds like CdSe NCs (76 meV) (figure 23C). This suggests that part of the broad PL band is intrinsic to the material, which is detrimental for its potential application in high-quality LEDs.

5.5. Conclusions

Different ensemble spectroscopy techniques and single particle spectroscopy strongly indicate that the broad PL bandwidth observed for CIS NCs partly arises due to inhomogeneities in the sample. PLE spectroscopy allows the interpretation of a subgroup of emitters in the sample, showing significantly decreased PL bandwidths. In addition, when cooling the sample to cryogenic temperatures the emission and PLE spectra remain unaffected supporting the put forward idea of the large size dispersion of the sample. Single particle spectroscopy substantiates this claim, by providing different single particle spectra with decreased FWHMs. The PL band width is decreased by 52% at a single particle level. Nevertheless, this reduced bandwidth is still considerably broader than observed for the conventional CdSe NCs. Even at the ensemble level CdSe/CdS core/shell NCs possess a narrower bandwidth by almost a factor of 3. This puts the application of CIS NCs for fluorophores for high quality LEDs far out. Improvement of the synthesis to reduce the size dispersion would benefit the application of CIS NCs in LSCs significantly. As a reduced PL bandwidth will decrease the absorption and emission overlap what will in turn minimize efficiency loss through reabsorption.

The nature of the broad intrinsic PL band is still not well-understood. Chapter 6 reports on the exciton recombination dynamics that are studied by power dependent transient absorption spectroscopy and power dependent emission spectroscopy.

5.6. Methods

Photoluminescence excitation spectroscopy. *The NCs were diluted in toluene and put in a cuvette. PLE spectra were measured on an Edinburgh Instrument FLS920 Spectrofluorimeter equipped with a 450 W Xenon lamp as excitation. The signal was detected with a Hamamatsu photosensor module H1072001.*

Single particle spectroscopy. *Single NCs emission spectra were put on a plasma-cleaned #1.5 coverslip inside a glovebox and sealed with UV-glue. The samples were excited using a 405nm ps-pulsed laser at a 250 kHz repetition rate.*

Temperature dependent spectroscopy. *The NCs were diluted in toluene and put in a cuvette. Photoluminescence and excitation spectra were measured on an Edinburgh Instrument FLS920 Spectrofluorimeter equipped with a 450 W Xenon lamp as excitation and a Hamamatsu R550-72 detector. PL decay curves were obtained by time-correlated single-photon counting on a Hamamatsu photosensor module H1072001. A pulsed diode 445nm laser at 50 kHz repetition rate was used as excitation source.*

6. Exciton recombination dynamics in $CuInS_2$

This chapter reports on the excited state dynamics in CIS nanocrystals using several ultrafast spectroscopy measurements. First, we provide a brief introduction to transient absorption. Followed by an outline of the current understanding of the exciton recombination pathway in CIS NCs. Chapter 6.2. reproduces the experimental proof for the two-fold degeneracy of the quantized electron in the CB, identifying the hole as the localized carrier in the exciton recombination process. The nature of the localization site is still under debate. Chapter 6.3. presents new arguments favouring the localization on Cu^+ ions. These findings are verified with power dependent emission spectroscopy measurements reported in chapter 6.4..

6.1. Introduction to transient absorption spectroscopy

The absorption and emission of photons is influenced by numerous dynamic processes, like Auger recombination, (bi)excitonic lifetime, and carrier localization, that proceed on extremely fast timescales. To study these fast-excited state processes transient absorption spectroscopy (TAS) is used. In TAS the sample under study is excited by a femtosecond pulsed laser also known as the pump. In the excited state, carriers occupy discrete energy levels. For an electron to be promoted from the VB to the CB upon photon absorption the corresponding energy levels in the excited state must be unoccupied. So, the excitons created by the pump pulse reduce the absorbance of the material. This phenomenon is also known as band edge bleaching. To record the bleach a second pulse, the probe pulse, is send to the sample after a delay time t with respect to the pump pulse (figure 22A). The probe pulse covers a wide spectrum of wavelengths and records changes in the NC absorption spectrum. In TAS the bleach is represented as a negative signal in the TA spectrum. Figure 22B shows the steady state absorption (A_0) (black), i.e. the absorption spectrum in the ground state, the band edge bleach ($\Delta A(t)$) (blue) and the excited state absorption spectrum ($A(t)$) (green). The positive TA signal at low energies arises when the probe pulse further excites an excited carrier. The unoccupied energy levels can be filled with new carriers causing the material to absorb more strongly than in the ground state. This phenomenon is also known as photo-induced absorption[85].

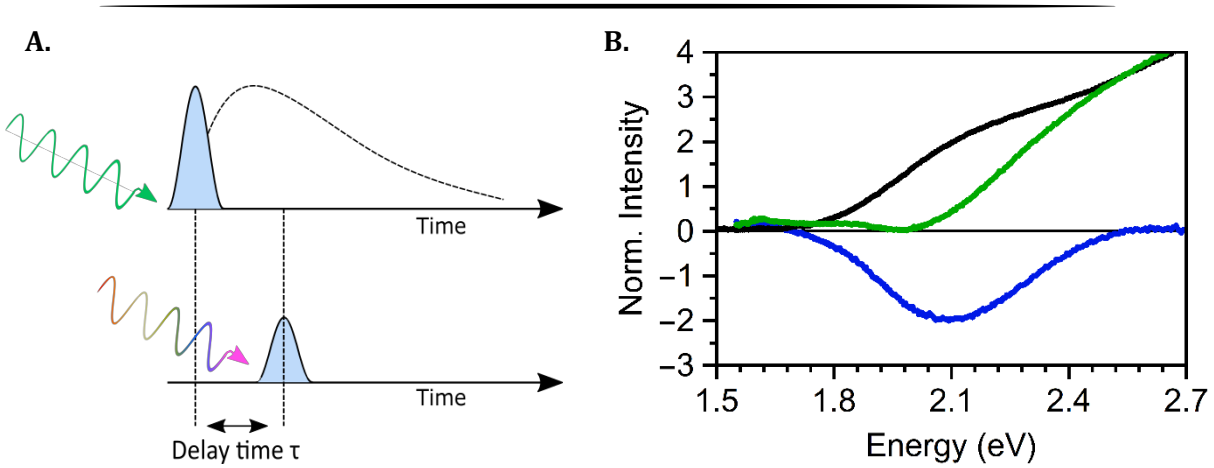

Figure 22 · A. Schematic representation of ultrafast pump-probe experiment. A pump pulse of a fixed wavelength excites the material. After a delay time t a second white light pulse probes the absorption spectrum of the excited sample. Occupation of the excited states lowers the absorption cross section reducing the absorption signal called bleaching. The bleach is a negative signal in the TA data. This figure was reproduced from ref[2]. **B.** Plot showing the steady state absorption (A_0) (black), the band edge bleach ($\Delta A(t)$) (blue) and the excited state absorption spectrum ($A(t)$) (green).

6.2. Carrier localization in excited CIS NCs

The CIS/CdS NCs are excited by a femtosecond pulsed 400nm laser, after which a broadband probe pulse records changes in the NC absorption spectrum at variable delay times. Different laser powers are used to excite the sample. Due to uncertainty of the spot size, the given excitation powers are no more than arbitrary units. Figure 23A shows the effect of different pump powers to the differential absorption spectrum (coloured) with respect to the steady state absorption spectrum (black). An increase in pump power increases the carrier population in the excited state thus increasing the bleaching of the steady state absorption spectrum. On the low energy side of the spectrum photo-induced absorption is observed when exciting the sample with strong laser powers. Figure 23B shows a TA spectral slice for the highest excitation power (blue), along with the steady state absorption spectrum (black), the second derivative of the steady state absorption (black dashed), the differential absorption spectrum (green) and PL spectrum (red). As mentioned before, the first minimum of the second derivative of the steady state absorption spectrum gives a good representation of the bandgap energy. The bleach signal is centred at the same position as the first minimum of the second derivative, this signal is therefore assigned to the first energy transition (excitation to the 1S state).

The bleach signal saturates with increasing pump power, indicating a finite occupation of exciton states involved in the band edge transition. Li et. al. shows that the electron state is two-fold degenerate[29]. The model the author of ref. [30] use is based on the assumptions that the pump energy is much greater than the bandgap and does not give rise to photo-induced absorption, and that the probability of generating an exciton is independent of the number of excitons already present in the NCs[86]. These assumptions result in the Poisson distribution of NC populations:

$$P(N) = \frac{\langle N \rangle^N e^{-\langle N \rangle}}{N!} \tag{12}$$

where P(N) is the probability of having N excitons in a NC when the average population of NCs is ⟨N⟩. The occupation numbers of the 1S state in this model can be calculated[86]:

$$n_{1S}^e = \frac{1}{2}P(1) + \sum_{i=2}^{\infty} P(i) \tag{13}$$

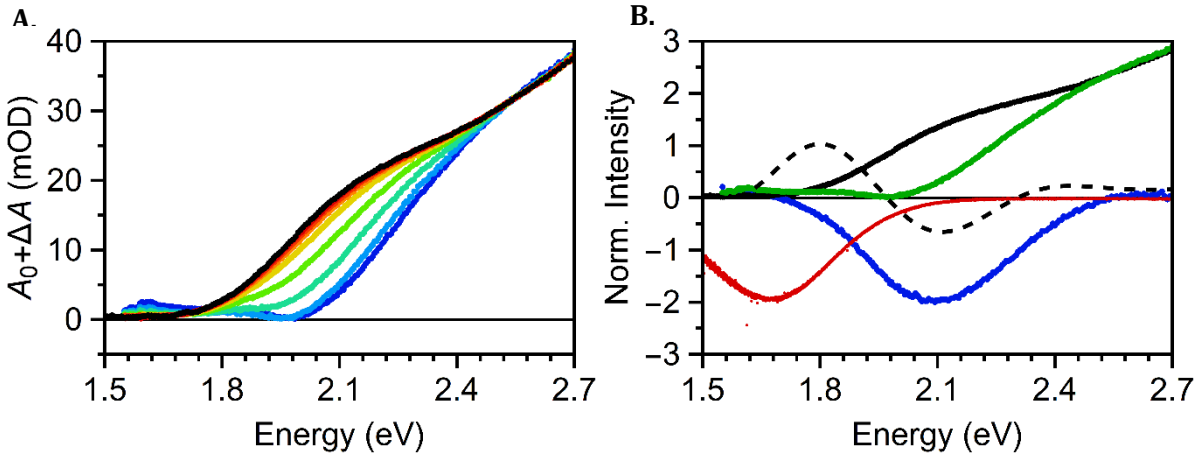

Figure 23 · A. The steady state absorption spectrum (black) and the excited state absorption spectrum for different pump powers (rainbow). Upon increasing the pump power more excitons are created, increasing the average occupation number, <N>, of the excited state. Filling of the excited state leads to bleaching of the interband optical transitions. **B.** The steady state absorption spectrum (A_0) (black), the second derivative of the steady state absorption (dashed), the excited state absorption spectrum ($A(\tau)$) (green), the differential spectrum (ΔA) (blue) and the emission spectrum (red) of $CuInS_2$/CdS.

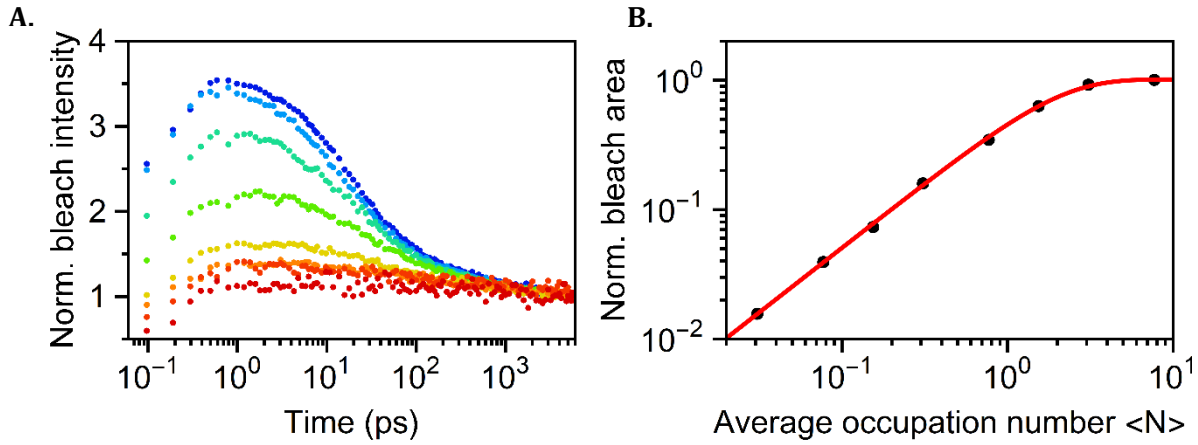

Figure 24 · A. The normalized bleach intensity for different excitation powers as a function of time. After ~1ps the intensity remains constant for low excitation powers indicating that the hot carriers have relaxed to the band edges. **B.** The normalized bleaching area, after 1ps, as a function of the pump-dependent average occupation number of the first excited state. Using Poisson statistics, a model could be fitted to the data showing the 2-fold degeneracy of the first exciton state.

For this model to provide an accurate relationship between the bleach signal and ⟨N⟩ all hot carriers must have relaxed to the band edge[86]. Figure 24A shows the bleach peak position as a function of time. After about 1ps the normalized bleach intensity remains constant. The normalized area of the bleach band is fitted as a function of the excitation power in order to calculate ⟨N⟩, as:

$$\langle N \rangle = \sigma * J \tag{14}$$

with J the photon fluence and σ the absorption cross section. In the fit we add an extra variable α to make up for the uncertainty of the fluence due to the arbitrary laser powers. Figure 24B shows the normalized bleach area as a function of ⟨N⟩ and a plot of Eq. 13. The experimental results show is consistent with the model, proving the two-fold degeneracy of one of the carrier states. Similar to CdSe the VB of CIS is three-fold degenerate and so a higher-level degeneracy is expected for the hole states. This is why the two-fold degenerate energy levels are assigned to the CB electrons, meaning that the localized carriers must be the holes. The nature of these localization sites, i.e. where the holes localize, is still unclear.

6.3. Hole localization on Cu^+ ions

The results above show that the localized carriers in the exciton recombination process in CIS NCs concern the holes, however, it is still under debate where these holes localize. Two independent studies by Knowles et al.[38] and Rice et al.[39] propose that the hole localizes on a Cu^+ ion. Both works base this claim on magnetic circular dichroism measurements, however, their interpretation of these results differs. In ref. [37][38] the authors find that paramagnetic Cu^{2+} ions are formed after excitation of the sample. They argue that the photogenerated hole localizes at a Cu^+ site creating the paramagnetic Cu^{2+} (d^9 configuration). According to the authors of ref. [40][39] the Cu^{2+} ions are already present in the material before excitation. More recent work by Berends et al.[30] finds discrepancies between the latter model and their own observations. No TA signal is observed when exciting the material with sub-bandgap-energies, which implies that no localized holes are present, or in negligible concentrations, prior to excitation. In addition, the authors of ref [39] observe different dynamics for the band edge bleaching and the photo-induced absorption, meaning that both signals originate from different charge carriers. For these reasons

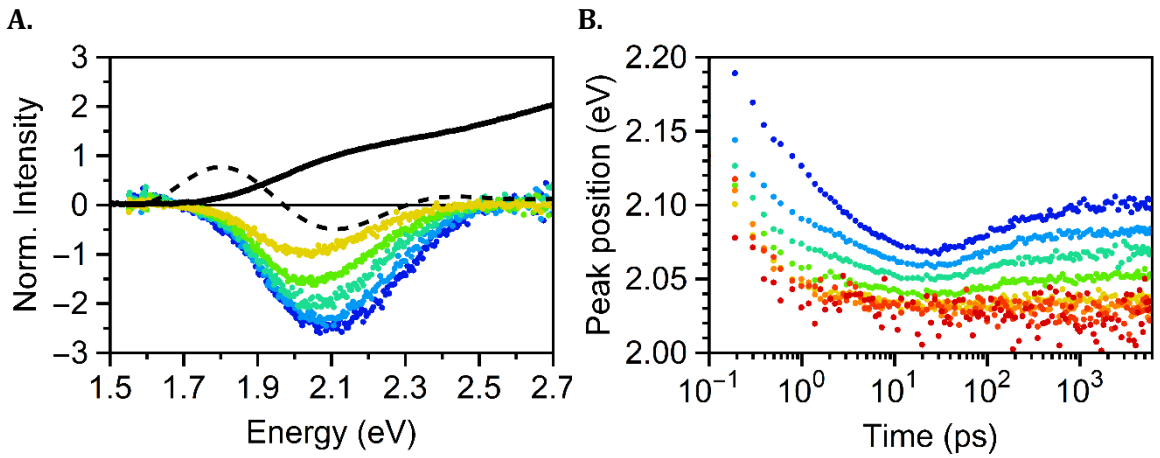

Figure 25 · A. Power dependence of the absorption band edge bleach plotted with the steady state absorption spectrum and its second derivative to show the clear blue shift upon increasing the excitation power. **B.** The bleach peak position plotted as a function of time. Higher excitation powers induce a longer initial red shift followed by an overall blue shift with respect to lower excitation powers.

---

they conclude that in the ground state Cu^{+} ions are present and Cu^{2+} only forms after photoexcitation, which consistent with

Figure 25A shows the power dependency of the absorption band edge signal after 6ns. A clear blue shift of the bleach signal is observed upon increasing the pump power. To our knowledge this shift has never been reported in literature before. At sub-ps time scales the peak position of the bleach signal redshifts as the hot carriers relax to the band edge. After ~1ps all carriers have relaxed for the lower pump powers and the bleach signal remains constant. Figure 25B plots the peak position as a function of time for different excitation powers. For higher pump powers the initial redshift due to intraband relaxation proceeds on an order of magnitude longer time scale. After ~20ps the redshift stagnates, and a blueshift occurs for the next 5ns. This blueshift is not observed when exciting the sample with lower laser powers. We hypothesize that in the multi-exciton regime the electron-hole pairs with a good wavefunction overlap recombine non-radiatively through Auger decay, leaving high energy excitons causing the blueshift. A similar blueshift when exciting the sample with higher laser powers, when looking at pump-push-probe (PPP) data. In a PPP experiment the sample is excited by a pump pulse, after a set time the sample is excited again by a second pulse, the push pulse. As the sample is excited again the ⟨N⟩ is temporally depleted causing a dip in the decay curve (figure 26) when probing the sample. The re-excited carriers cool again to the band edges and the dip recovers to the decay curve observed for the pump-probe experiments. The decay curves of the PPP experiments for different push powers do, however, not recover to the same ⟨N⟩. The peak position of the bleach also shifts after the push pulse. This shift is observable when plotting the differential spectrum of the bleach signals before and after the push pulse and compare it with the case as if there is no push pulse (figure 26). We propose that the push pulse excites the hole back into the VB from where they localize again on Cu^{+} centres creating a new distribution of the excitons. Redistribution will facilitate Auger decay for the excitons with a good overlap of the wavefunctions, leaving the high energy excitons causing the blueshift. For this hypothesis to hold the PL band should also blueshift upon increasing the excitation power.

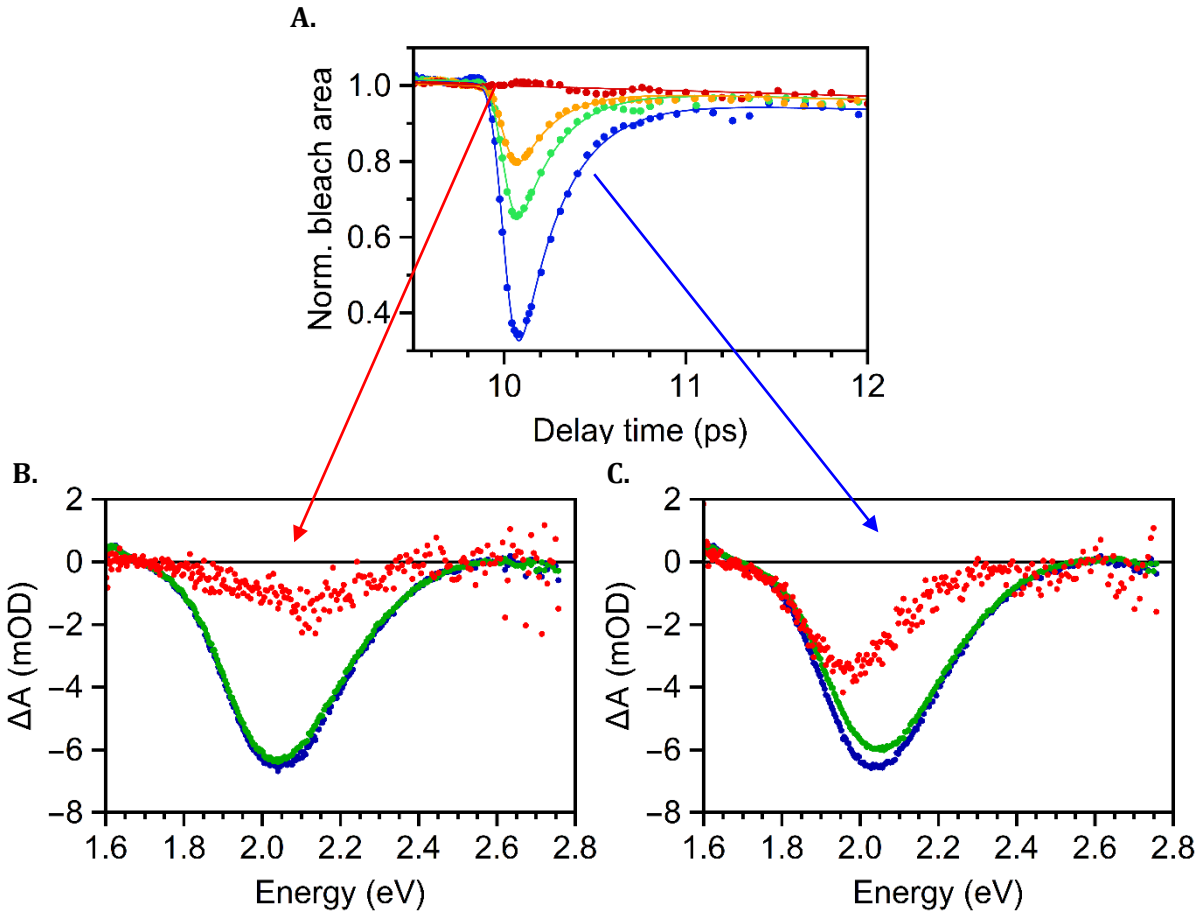

Figure 26 · A. PPP decay trace plotted as a function of delay time t. Temporal depletion of the excited state due to the push pulse causes a dip in the decay trace. **B.** The TA signal before (blue) and after (green) the push and the differential spectrum (red) as if there was no push. **C.** The TA signal before (blue) and after (green) the push and the differential spectrum (red) for the highest push power showing a clear blueshift after the pulse. Both differential spectra are multiplied by a factor of 5 to emphasize the bleach shift.

6.4. Power dependent emission spectroscopy

Using a 405 nm continuous wave laser the CIS/CdS core/shell NCs are excited. For repeated low laser powers PL measurements, the signal remains constant, however, for increased laser powers the emission signal blue shifts (figure 27). These findings support the idea that in the multi-exciton regime Auger decay depletes the electron-hole pairs with good wavefunction overlap. To validate this idea these experiments, have to be repeated using different core/shell NCs. The experiments described in chapter 5 show that this particular CIS/CdS core/shell NCs sample has a large NC size dispersion. So, one could also argue that in the multi-exciton regime the blueshift arises due to the saturation of the absorption cross section of large absorbers. This would also explain the longer-lived initial redshift observed for higher excitation powers in figure 25B.

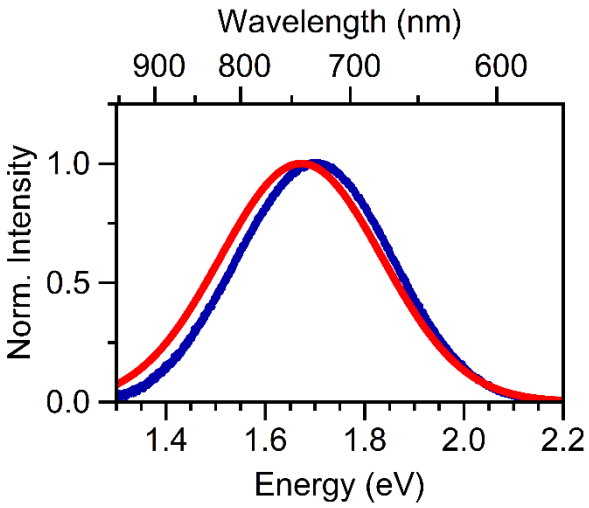

Figure 27 · PL spectra of CIS recorded for different excitation powers. Upon increasing the excitation power, the emission feature blue shifts.

6.4. Conclusions

From the TA data acquired from CIS/CdS core/shell NCs the experimental prove for the two-fold degeneracy of the CB electrons in the excited state of CIS NCs is reproduced. The model to describe the relationship between the bleach signal and the average occupation number of excitons in CdSe NCs holds for CIS NCs as well. Similar to CdSe the VB of CIS is three-fold degenerate and so a higher-level degeneracy is expected for the hole states. This is why the two-fold degenerate energy levels are assigned to the CB electrons, meaning that the localized carriers must be the holes. The recombination dynamics of are studied using power dependent pump-probe and pump-push-probe experiments. The pump-probe data shows a blueshift of the bleach signal upon increasing the pump power. We attribute this shift to fast non-radiative Auger recombination of e-h pairs with a good wavefunction overlap in the multi-exciton regime, leaving the energetically higher excitons thus shifting the bleach signal to the blue. A similar trend is observed for the PPP data where the bleach signal is blueshifted upon increasing the push pulse. To support this idea, power dependent emission measurements are performed, showing a blueshift of the PL band upon increasing the excitation power as well.

To validate this idea the experiment described above have to be repeated using different core/shell samples. The experiments described in chapter 5 show that this particular CIS/CdS core/shell NCs sample has a large NC size dispersion. So, one could argue that in the multi-exciton regime the blueshift arises due to the saturation of the absorption cross section of large absorbers. Power dependent TRES measurements could also provide insight in the recombination dynamics. If our hypothesis holds a blueshift of the PL peak should be observed over time for high excitation powers. Furthermore, to rule out different recombination mechanisms the localization sites should be identified using sophisticated techniques like electron paramagnetic resonance.

6.5. Methods

Transient absorption spectroscopy. *The CIS/CdS core/shell NCs were diluted with toluene and stored in a cuvette. Without stirring the sample was excited with a 400 nm pulsed fs-laser.*

Power dependent emission spectroscopy. *The CIS/CdS core/shell NCs were diluted with toluene and stored in a special cuvette that allows stirring of the sample without being detected. The samples were excited using a 405nm ps-pulsed laser at different arbitrary powers.*

7. Conclusions

We set out to explore a relatively new synthesis method to obtain more control over the InP NC synthesis. By creating a spherical quantum well, we hypothesized the upper size limit associated with current synthesis methods could be circumvented. Furthermore, a narrower size dispersion was expected due to the shell by shell overgrowth approach. Despite promising results found in literature, the synthesis was not a success. Instead of InP shells, new nuclei were formed during the reaction and the reactive TBP-In precursor even dissolved the ZnSe core NCs. For future research efforts one should begin looking into different cation and/or anion precursors in order to find a better-balanced reactivity towards the core NCs and between the precursors. Once these precursors are identified and monodisperse ZnSe/InP core/shell NCs are obtained, the method could be upscaled by using a slow injection method instead of SILAR. Slow injection would improve the scalability of the synthesis which is beneficial for potential application of InP in high quality lighting and LEDs.

To study the nature of the broad PL band observed for CIS NCs and the exciton recombination pathway CIS cores, CIS/ZnS and CIS/CdS core/shell NCs were synthesized. The crystal structure, size and shape of the CIS NCs were determined using HAADF-STEM, SAXS, WAXS and absorption spectroscopy. Despite the weak contrast obtained with HAADF-WAXS, the images clearly proved the tetragonal crystal structure of CIS NCs. Based on X-ray crystallography data the crystalline domain and radius of gyration of CIS NCs were approximated. From these quantities the edge length of tetrahedral shape was calculated, ~4.9nm. The increased scale of the core/shell NC synthesis did not affect the optoelectronic properties of CIS NCs much. The redshift and decreased intensity of the PL band was attributed to an increased shell thickness causing the core electron to delocalize into the CdS shell forming a Type-I$^{1/2}$ energy band alignment. The synthesis of thick shell CIS/CdS core/shell NCs substantiated this claim as the PL decay rate increased hence lowering the PLQY.

Various ensemble techniques and single particle spectroscopy experiments were performed to assess the nature of the broad bandwidth commonly observed for CIS NCs. For these measurements we used CIS/CdS core/shell NCs we decided to use the scaled-up CIS/CdS core/shell NCs. As the CdS shell enhances the optoelectronic properties of CIS NCs while conserving the CIS (nano)crystal structure. The ensemble techniques strongly indicate an inhomogeneous nature of the line broadening for CIS NCs. The strong reduction of the FWHM recorded for single CIS NCs proves the optoelectronic properties can still be significantly improved by synthesis of monodisperse NCs. Nevertheless, this reduced bandwidth is still considerably broader than observed for the conventional CdSe NCs. Even at the ensemble level CdSe/CdS core/shell NCs possess a narrower bandwidth by almost a factor of 3. This puts the application of CIS NCs for fluorophores for high quality LEDs far out. Improvement of the synthesis to reduce the size dispersion would benefit the application of CIS NCs in LSCs significantly. As a reduced PL bandwidth will decrease the absorption and emission overlap what will in turn minimize efficiency loss through reabsorption.

From the TA data acquired from CIS/CdS core/shell NCs the experimental prove for the two-fold degeneracy of the CB electrons in the excited state of CIS NCs is reproduced. Moreover, new insights on the exciton recombination pathway in CIS NCs are provided. The pump-probe data for different excitation powers shows a blueshift of the bleach signal upon increasing the pump power. We attribute this shift to fast non-radiative Auger recombination of e-h pairs with a good wavefunction overlap in the multi-exciton regime, leaving the energetically higher excitons thus shifting the bleach signal to the blue. A similar trend is observed for the PPP data where the bleach

signal is blueshifted upon increasing the push pulse. To support this idea, power dependent emission measurements are performed, showing a blueshift of the PL band upon increasing the excitation power as well.

To validate this idea the experiment described above have to be repeated using different core/shell samples. The experiments described in chapter 5 show that this particular CIS/CdS core/shell NCs sample has a large NC size dispersion. So, one could argue that in the multi-exciton regime the blueshift arises due to the saturation of the absorption cross section of large absorbers. Power dependent TRES measurements could also provide insight in the recombination dynamics. If our hypothesis holds a blueshift of the PL peak should be observed over time for high excitation powers. Furthermore, to rule out different recombination mechanisms the localization sites should be identified using sophisticated techniques like electron paramagnetic resonance.

References

1. Donegá, C. de M. Synthesis and properties of colloidal heteronanocrystals. *Chem. Soc. Rev.* **40**, 1512–1546 (2011).

2. Rabouw, F. T. Before there was light. (Utrecht University, 2015).

3. Xu, J. *et al.* 2D matrix engineering for homogeneous quantum dot coupling in photovoltaic solids. *Nat. Nanotechnol.* **13**, 456–462 (2018).

4. Bourzac, K. Quantum dots go on display. *Nature* **493**, 283 (2013).

5. Kagan, C. R., Lifshitz, E., Sargent, E. H. & Talapin, D. V. Building devices from colloidal quantum dots. *Science (80-.).* **353**, (2016).

6. Berends, A. C., Mangnus, M. J. J., Xia, C., Rabouw, F. T. & de Mello Donega, C. Optoelectronic Properties of Ternary I–III–VI 2 Semiconductor Nanocrystals: Bright Prospects with Elusive Origins. *J. Phys. Chem. Lett.* **10**, 1600–1616 (2019).

7. Burda, C., Chen, X., Narayanan, R. & El-Sayed, M. A. *Chemistry and properties of nanocrystals of different shapes*. *Chemical Reviews* **105**, (2005).

8. Roduner, E. Size matters: why nanomaterials are different. *Chem. Soc. Rev.* **35**, 583 (2006).

9. Alivisatos, A. P. Perspectives on the physical chemistry of semiconductor nanocrystals. *J. Phys. Chem.* **100**, 13226–13239 (1996).

10. Wu, K., Li, H. & Klimov, V. I. Tandem luminescent solar concentrators based on engineered quantum dots. *Nat. Photonics* **12**, 105–110 (2018).

11. Tyagi, P. & Subramony, J. A. Nanotherapeutics in oral and parenteral drug delivery: Key learnings and future outlooks as we think small. *J. Control. Release* **272**, 159–168 (2018).

12. Liu, H. *et al.* Oral administration of highly bright Cr 3+ doped ZnGa 2 O 4 nanocrystals for in vivo targeted imaging of orthotopic breast cancer. *J. Mater. Chem. B* **6**, 1508–1518 (2018).

13. Bi, Y. *et al.* Infrared Solution-Processed Quantum Dot Solar Cells Reaching External Quantum Efficiency of 80% at 1.35 μm and Jsc in Excess of 34 mA cm−2. *Adv. Mater.* **30**, 1–6 (2018).

14. Chen, B., Pradhan, N. & Zhong, H. From Large-Scale Synthesis to Lighting Device Applications of Ternary I-III-VI Semiconductor Nanocrystals: Inspiring Greener Material Emitters. *J. Phys. Chem. Lett.* **9**, 435–445 (2018).

15. Brus, L. E. Electron–electron and electron-hole interactions in small semiconductor crystallites: The size dependence of the lowest excited electronic state. *J. Chem. Phys.* **80**, 4403–4409 (1984).

16. Wang, H., De Mello Donegá, C., Meijerink, A. & Glasbeek, M. Ultrafast exciton dynamics in CdSe quantum dots studied from bleaching recovery and fluorescence transients. *J. Phys. Chem. B* **110**, 733–737 (2006).

17. Klimov, V. I. Spectral and Dynamical Properties of Multiexcitons in Semiconductor Nanocrystals. *Annu. Rev. Phys. Chem* **58**, 635–73 (2007).

18. Guyot-Sionnest, P. & Pandey, A. Slow Electron Cooling in Colloidal. *Science* **322**, 929–932 (2008).

19. Hannah, D. C. *et al.* Observation of size-dependent thermalization in CdSe nanocrystals

using time-resolved photoluminescence spectroscopy. *Phys. Rev. Lett.* **107**, 13–16 (2011).

20. Efros, A. L. *et al.* Band-edge exciton in quantum dots of semiconductors with a degenerate valence band: Dark and bright exciton states. *Phys. Rev. B - Condens. Matter Mater. Phys.* **54**, 4843–4856 (1996).

21. Shabaev, A., Rodina, A. V. & Efros, A. L. Fine structure of the band-edge excitons and trions in CdSe/CdS core/shell nanocrystals. *Phys. Rev. B - Condens. Matter Mater. Phys.* **86**, 1–14 (2012).

22. Rabouw, F. T. & de Mello Donega, C. Excited-State Dynamics in Colloidal Semiconductor Nanocrystals. *Top. Curr. Chem.* **374**, 1–30 (2016).

23. Cragg, G. E. & Efros, A. L. Suppression of Auger Processes in Confined Structures. *Nano Lett.* **10**, 313–317 (2010).

24. Climente, J. I., Movilla, J. L. & Planelles, J. Auger Recombination Suppression in Nanocrystals with Asymmetric Electron-Hole Confinement. *Small* **8**, 754–759 (2012).

25. Reiss, P., Protière, M. & Li, L. Core/shell semiconductor nanocrystals. *Small* **5**, 154–168 (2009).

26. Pandey, A. & Guyot-Sionnest, P. Intraband spectroscopy and band offsets of colloidal II-VI core/shell structures. *J. Chem. Phys.* **127**, 104710 (2007).

27. De Mello Donegá, C. Formation of nanoscale spatially indirect excitons: Evolution of the type-II optical character of CdTe/CdSe heteronanocrystals. *Phys. Rev. B - Condens. Matter Mater. Phys.* **81**, 1–20 (2010).

28. Cuins, M. P. *et al.* Noninjection Gram-Scale Synthesis of. **4**, 5253–5262 (2010).

29. Li, L. *et al.* Efficient Synthesis of Highly Luminescent Copper Indium Sulfide-Based Core/Shell Nanocrystals with Surprisingly Long-Lived Emission. *J. Am. Chem. Soc.* **133**, 1176–1179 (2011).

30. Berends, A. C. *et al.* Radiative and Nonradiative Recombination in CuInS 2 Nanocrystals and CuInS 2 -Based Core/Shell Nanocrystals. *J. Phys. Chem. Lett.* **7**, 3503–3509 (2016).

31. Zhang, S. B., Wei, H.-H., Zunger, A. & Katayama-Yoshida, H. Defect physics of the CuInSe2 chalcopyrite semiconductor. *J. Phys. Chem. Solids* **60**, 1865–1873 (1999).

32. Ueng, H. Y. & Hwang, H. L. The defect structure of CuInS2. part I: Intrinsic defects. *J. Phys. Chem. Solids* **50**, 1297–1305 (1989).

33. Jaffe, J. E. & Zunger, A. Electronic structure of the ternary chalcopyrite semiconductors CuAlS2, CuGaS2, CuInS2, CuAlSe2, CuGaSe2, and CuInSe2. *Phys. Rev. B* **28**, 5822–5847 (1983).

34. Kolny-Olesiak, J. & Weller, H. Synthesis and application of colloidal CuInS2 semiconductor nanocrystals. *ACS Appl. Mater. Interfaces* **5**, 12221–12237 (2013).

35. Binsma, J. J. M., Giling, L. J. & Bloem, J. Luminescence of CuInS2. *J. Lumin.* **27**, 35–53 (1982).

36. Omata, T., Nose, K., Kurimoto, K. & Kita, M. Electronic transition responsible for size-dependent photoluminescence of colloidal CuInS2 quantum dots. *J. Mater. Chem. C* **2**, 6867–6872 (2014).

37. Kraatz, I. T., Booth, M., Whitaker, B. J., Nix, M. G. D. & Critchley, K. Sub-bandgap emission and intraband defect-related excited-state dynamics in colloidal CuInS2/ZnS quantum

dots revealed by femtosecond pump-dump-probe spectroscopy. *J. Phys. Chem. C* **118**, 24102–24109 (2014).

38. Knowles, K. E., Nelson, H. D., Kilburn, T. B. & Gamelin, D. R. Singlet–Triplet Splittings in the Luminescent Excited States of Colloidal Cu + :CdSe, Cu + :InP, and CuInS 2 Nanocrystals: Charge-Transfer Configurations and Self-Trapped Excitons. *J. Am. Chem. Soc.* **137**, 13138–13147 (2015).

39. Rice, W. D., McDaniel, H., Klimov, V. I. & Crooker, S. A. Magneto-Optical Properties of CuInS 2 Nanocrystals. *J. Phys. Chem. Lett.* **5**, 4105–4109 (2014).

40. Knowles, K. E. *et al.* Luminescent Colloidal Semiconductor Nanocrystals Containing Copper: Synthesis, Photophysics, and Applications. *Chem. Rev.* **116**, 10820–10851 (2016).

41. Tamang, S., Lincheneau, C., Hermans, Y., Jeong, S. & Reiss, P. Chemistry of InP Nanocrystal Syntheses. *Chem. Mater.* **28**, 2491–2506 (2016).

42. Mićić, O. I., Curtis, C. J., Jones, K. M., Sprague, J. R. & Nozik, A. J. Synthesis and characterization of InP quantum dots. *J. Phys. Chem.* **98**, 4966–4969 (1994).

43. Gary, D. C., Terban, M. W., Billinge, S. J. L. & Cossairt, B. M. Two-step nucleation and growth of InP quantum dots via magic-sized cluster intermediates. *Chem. Mater.* **27**, 1432–1441 (2015).

44. Xu, S., Kumar, S. & Nann, T. Rapid synthesis of high-quality InP nanocrystals. *J. Am. Chem. Soc.* **128**, 1054–1055 (2006).

45. Graichen, P. *Current and Future Cost of Photovoltaics. Long-term Scenarios for Market Development, System Prices and LCOE of Utility-Scale PV Systems*. (2015). doi:059/01-S-2015/EN

46. Parliament, E. *Directive (EU) 2018/844 of the European Parliament and the Council on the energy performance of buildings*. (2018).

47. Weber, W. H. & Lambe, J. Luminescent greenhouse collector for solar radiation. *Appl. Opt.* **15**, 2299 (1976).

48. Debije, M. G. & Verbunt, P. P. C. Thirty years of luminescent solar concentrator research: Solar energy for the built environment. *Adv. Energy Mater.* **2**, 12–35 (2012).

49. van Sark, W. G. J. H. M. Luminescent solar concentrators - A low cost photovoltaics alternative. *Renew. Energy* **49**, 207–210 (2013).

50. Batchelder, J. S., Zewai, A. H. & Cole, T. Luminescent solar concentrators 1: Theory of operation and techniques for performance evaluation. *Appl. Opt.* **18**, 3090 (1979).

51. Meinardi, F. *et al.* Highly efficient luminescent solar concentrators based on earth-Abundant indirect-bandgap silicon quantum dots. *Nat. Photonics* **11**, 177–185 (2017).

52. Bradshaw, L. R., Knowles, K. E., Mcdowall, S. & Gamelin, D. R. Nanocrystals for Luminescent Solar Concentrators. (2015). doi:10.1021/nl504510t

53. Pietryga, J. M. *et al.* Spectroscopic and Device Aspects of Nanocrystal Quantum Dots. *Chem. Rev.* **116**, 10513–10622 (2016).

54. Currie, M. J., Mapel, J. K., Heidel, T. D., Goffri, S. & Baldo, M. A. High-efficiency organic solar concentrators for photovoltaics. *Science (80-.).* **321**, 226–228 (2008).

55. Aeberhard, U., Vaxenburg, R., Lifshitz, E. & Tomić, S. Fluorescence of colloidal PbSe/PbS

QDs in NIR luminescent solar concentrators. *Phys. Chem. Chem. Phys.* **14**, 16223–16228 (2012).

56. Meinardi, F. *et al.* Large-area luminescent solar concentrators based on Stokes-shift-engineered nanocrystals in a mass-polymerized PMMA matrix. *Nat. Photonics* **8**, 392–399 (2014).

57. Christodoulou, S. *et al.* Synthesis of highly luminescent wurtzite CdSe/CdS giant-shell nanocrystals using a fast continuous injection route. *J. Mater. Chem. C* **2**, 3439–3447 (2014).

58. Brovelli, S. *et al.* Electrochemical Control of Two-Color Emission from Colloidal Dot-in-Bulk Nanocrystals. *Nano Lett.* **14**, 3855–3863 (2014).

59. Galland, C. *et al.* Dynamic hole blockade yields two-color quantum and classical light from dot-in-bulk nanocrystals. *Nano Lett.* **13**, 321–328 (2013).

60. Parliament, E. *Directive 2011/65/EU of the European Parliament and of the Council of8 June 2011 On the Restriction of the Use of Certain Hazardous Substances in Electrical and Electronic Equipment*. (2011).

61. Colvin, V. L., Schlamp, M. C. & Alivisatos, A. P. Light-emitting diodes made from cadmium selenide nanocrystals and a semiconducting polymer. *Nature* **370**, 775–776 (1994).

62. Oliver, J. Quantum Dots: Global Market Growth and Future Commercial Prospects. *BBC Research* (2011).

63. Shirasaki, Y., Supran, G. J., Bawendi, M. G. & Bulović, V. Emergence of colloidal quantum-dot light-emitting technologies. *Nat. Photonics* **7**, 13–23 (2013).

64. Grim, J. Q., Manna, L. & Moreels, I. A sustainable future for photonic colloidal nanocrystals. *Chem. Soc. Rev.* **44**, 5897–5914 (2015).

65. Dupont, D., Tessier, M. D., Smet, P. F. & Hens, Z. Indium Phosphide-Based Quantum Dots with Shell-Enhanced Absorption for Luminescent Down-Conversion. *Adv. Mater.* **29**, 1–6 (2017).

66. Jeong, B. G. *et al.* Colloidal Spherical Quantum Wells with Near-Unity Photoluminescence Quantum Yield and Suppressed Blinking. *ACS Nano* **10**, 9297–9305 (2016).

67. Dennis, A. M., Saeboe, A. M., Kays, J. C. & Mahler, A. H. Pushing indium phosphide quantum dot emission deeper into the near infrared. in *Colloidal Nanoparticles for Biomedical Applications XIII* (eds. Liang, X.-J., Parak, W. J. & Osiński, M.) **10507**, 40 (SPIE, 2018).

68. Kim, S. *et al.* Reverse Type-I ZnSe/InP/ZnS Core/Shell/Shell Nanocrystals: Cadmium-Free Quantum Dots for Visible Luminescence. *Small* **7**, 70–73 (2011).

69. Groeneveld, E. *et al.* Tailoring ZnSe–CdSe Colloidal Quantum Dots via Cation Exchange: From Core/Shell to Alloy Nanocrystals. *ACS Nano* **7**, 7913–7930 (2013).

70. Eilers, J., van Hest, J., Meijerink, A. & Donega, C. D. M. Unravelling the Size and Temperature Dependence of Exciton Lifetimes in Colloidal ZnSe Quantum Dots. *J. Phys. Chem. C* **118**, 23313–23319 (2014).

71. Ivanov, S. A. *et al.* Type-II Core/Shell CdS/ZnSe Nanocrystals: Synthesis, Electronic Structures, and Spectroscopic Properties. *J. Am. Chem. Soc.* **129**, 11708–11719 (2007).

72. Xia, C. *et al.* Size-dependent band-gap and molar absorption coefficients of colloidal CuInS2 quantum dots. *ACS Nano* **12**, 8350–8361 (2018).

73. Zang, H. *et al.* Thick-Shell CuInS 2 /ZnS Quantum Dots with Suppressed “Blinking” and Narrow Single-Particle Emission Line Widths. *Nano Lett.* **17**, 1787–1795 (2017).

74. De Trizio, L. *et al.* Strongly fluorescent quaternary Cu-In-Zn-S nanocrystals prepared from Cu 1-xInS 2 nanocrystals by partial cation exchange. *Chem. Mater.* **24**, 2400–2406 (2012).

75. Huang, L. *et al.* Cadmium- and zinc-alloyed Cu-In-S nanocrystals and their optical properties. *J. Nanoparticle Res.* **15**, (2013).

76. Hens, Z. & Moreels, I. Light absorption by colloidal semiconductor quantum dots. *J. Mater. Chem.* **22**, 10406 (2012).

77. Maes, J. *et al.* Size and concentration determination of colloidal nanocrystals by small-angle x-ray scattering. *Chem. Mater.* **30**, 3952–3962 (2018).

78. Burnett, J. D. *et al.* Structure-property relationships along the Fe-substituted CuInS2 series: Tuning of thermoelectric and magnetic properties. *Mater. Chem. Phys.* **147**, 17–27 (2014).

79. Langford, J. I. & Wilson, A. J. C. Scherrer after sixty years: A survey and some new results in the determination of crystallite size. *J. Appl. Crystallogr.* **11**, 102–113 (1978).

80. Scherrer, P. Bestimmung der inneren Struktur und der GröBe von Kolloidteilchen mittels Röntgenstrahlen. *Göttinger Nachrichten Gesell.* **2**, 98 (1918).

81. Keshari, A. K. & Pandey, A. C. Size and Distribution: A Comparison of XRD, SAXS and SANS Study of II–VI Semiconductor Nanocrystals. *J. Nanosci. Nanotechnol.* **8**, 1221–1227 (2008).

82. Janke, E. M. *et al.* Origin of Broad Emission Spectra in InP Quantum Dots: Contributions from Structural and Electronic Disorder. *J. Am. Chem. Soc.* **140**, 15791–15803 (2018).

83. Valerini, D. *et al.* Temperature dependence of the photoluminescence properties of colloidal CdSeZnS core/shell quantum dots embedded in a polystyrene matrix. *Phys. Rev. B - Condens. Matter Mater. Phys.* **71**, 1–6 (2005).

84. Efros, A. L. & Rosen, M. The Electronic Structure of Semiconductor Nanocrystals. *Annu. Rev. Mater. Sci.* **30**, 475–521 (2000).

85. Berends, A. C. Explorations in nanoscale copper indium sulfide. (Utrecht University, 2018).

86. Klimov, V. I. Optical Nonlinearities and Ultrafast Carrier Dynamics in Semiconductor Nanocrystals. *J. Phys. Chem. B* **104**, 6112–6123 (2000).